AD_____

Award Number: W81XWH-08-1-0127

TITLE: Accurate and Fast Localization of Prostate for External Beam Radiation Therapy

PRINCIPAL INVESTIGATOR: Jing Wang, Ph.D.

CONTRACTING ORGANIZATION: Stanford University
Stanford, CA 94305

REPORT DATE: March 2009

TYPE OF REPORT: Annual Summary

PREPARED FOR: U.S. Army Medical Research and Materiel Command
Fort Detrick, Maryland 21702-5012

REPORT DOCUMENTATION PAGE

Form Approved
OMB No. 0704-0188

1. REPORT DATE *(dd-mm-yyyy)*	2. REPORT TYPE	3. DATES COVERED *(From - To)*
12-03-2009	Annual Summary	15 Feb 2008- 14 Feb 2009

4. TITLE AND SUBTITLE

Accurate and Fast Localization of Prostate for External Beam Radiation Therapy

5a. CONTRACT NUMBER

5b. GRANT NUMBER
W81XWH-08-1-0127

5c. PROGRAM ELEMENT NUMBER

6. AUTHOR(S)

Jing Wang, Ph.D.

5d. PROJECT NUMBER

5e. TASK NUMBER

5f. WORK UNIT NUMBER

7. PERFORMING ORGANIZATION NAME(S) AND ADDRESS(ES)

Stanford University
Stanford, CA 94305

8. PERFORMING ORGANIZATION REPORT NUMBER

9. SPONSORING / MONITORING AGENCY NAME(S) AND ADDRESS(ES)

10. SPONSOR/MONITOR'S ACRONYM(S)

11. SPONSOR/MONITOR'S REPORT NUMBER(S)

12. DISTRIBUTION / AVAILABILITY STATEMENT

Approved for public release; distribution unlimited

13. SUPPLEMENTARY NOTES

14. ABSTRACT

The development of intensity modulated radiation therapy (IMRT) makes it possible to deliver high precision conformal dose distributions to the target. However, the non-rigid internal motion of the prostate makes it difficult to locate the target precisely during IMRT. In this project, we propose to develop a tomosynthesis-based method for fast and accurate prostate localization during IMRT. The hypothesis of this proposal is that the effective use of 3D information provided by tomosynthesis and the development of a non-rigid tomosynthesis/CT registration technique will enable us to significantly improve the precision of prostate target localization. We have carried a systematic study on the tomosynthesis based prostate localization technique. A number of important milestones have been accomplished, which include (i) implemented a ray-tracing based projector to generate projection data from a digital phantom and analytical FDK image reconstruction algorithm to reconstruct tomosynthesis image; (ii) Developed a statistics –based sinogram smoothing algorithm to suppress noise in projection data and improve image quality in reconstructed image; and (iii) Developed an iterative image reconstruction algorithm with a new prior constraint to improve image quality and resolution in tomographic images. It is expected that these tools will improve the accuracy of the prostate localization for EBRT.

15. SUBJECT TERMS

Prostate Cancer

16. SECURITY CLASSIFICATION OF:			17. LIMITATION OF ABSTRACT	18. NUMBER OF PAGES	19a. NAME OF RESPONSIBLE PERSON
a. REPORT	b. ABSTRACT	c. THIS PAGE		47	19b. TELEPHONE NUMBER *(include area code)*

Table of Contents

Page

I. Introduction

This Postdoctoral Training Award (W81XWH-08-1-0127, entitled "Accurate and Fast Localization of Prostate for External Beam Radiation Therapy") was awarded to the principal investigator (PI) for the period of February 15, 2008 --- February 14, 2010. This is the annual report for the first funding period (February 15, 2008 --- February 14, 2009). The purpose of this project is to develop a tomosynthesis-based method for fast and accurate prostate localization during IMRT. The specific aims of this project are: 1) To determine the protocol for acquiring projection data for tomosynthesis, 2) to determine the optimal tomosynthetic image reconstruction algorithm, 3) to determine an accurate non-rigid registration method for registering the daily tomosynthetic images to the planning CT images of the prostate, 4) to develop and evaluate the tomosynthesis-based repositioning protocols. Under the generous support from the U.S. Army Medical Research and Materiel Command (USAMRMC), the PI has contributed significantly to the field of prostate cancer research by applying the physics and engineering knowledge. A number of conference abstracts and refereed journal publications have been resulted from the support. In this report, the past year's research activities of the PI are highlighted.

II. Body

During the past year, the PI has successfully implemented a ray-tracing method to generate the projection image from a digital mathematical phantom and used Trilogy oncology system to acquire projection data of an anthropomorphic phantom with various protocols. The PI has also implemented tomographic image reconstruction algorithms including both analytical filtered back-projection (FBP)-type method and statistics-based iterative image reconstruction algorithm. The analytical image reconstruction algorithm is based on the widely-used Feldkamp Davis and Kress (FDK) algorithm. To enhance the image of reconstructed tomographic image, a statistics-base sinogram smoothing algorithm has been developed. Two journal papers (ref.1 and 2) and a conference proceeding (ref. 3) have been published based on the developed algorithm. The iterative image reconstruction algorithm is based on statistical properties of measured projection data, where the noise modeling of measured data is incorporated into the penalized weighted least-squares objective function. To improve the image resolution of reconstructed image, a new prior model is proposed. One conference abstract (ref.4) and one journal paper (ref. 5) have been published based the proposed algorithm. Currently, the PI is conducting research on image reconstruction and registration for tomosynthesis using few projections from the cone-beam CT. One paper regarding the number of projection required for accurate tomosynthetic image reconstruction and registration is under preparation.

III. Key Research Accomplishments

- Developed a simulation package: including projector to generate projection image from a digital mathematical phantom and FDK reconstruction algorithm to reconstruct tomosynthesis image.
- Developed a statistics –based sinogram smoothing algorithm to suppress noise in projection data and improve image quality in reconstructed image.

- Developed an iterative image reconstruction algorithm with a new prior constraint to improve image quality and resolution in tomographic images.

IV. Reportable Outcomes

The following is a list of publications resulted from the grant support in the last funding period.

Refereed Publications:

1. **J. Wang**, L. Zhu, and L. Xing, "Noise reduction in low-dose X-ray fluoroscopy for Image Guided Radiation Therapy (IGRT)", *Int J Radiat Oncol Biol Phys*, in press, 2009
2. **J. Wang**, T. Li, and L. Xing, "Iterative image reconstruction for CBCT using edge-preserving prior", *Medical Physics*, vol. 36, pp. 252-260, 2009
3. L. Zhu, **J. Wang**, and L. Xing, "Noise suppression in scatter correction for Cone-Beam CT", *Medical Physics*, vol. 36, pp. 741-752, 2009
4. **J. Wang**, T. Li, Z. Liang and L. Xing, "Dose reduction for kilovoltage cone-beam computed tomography in radiation therapy", *Physics in Medicine and Biology*, vol. 53, pp. 2897-2909, 2008

Conference Abstract:

1. **J. Wang**, A. Chai, L. Xing, "Noise correlation in CBCT projection data and its application for noise reduction in low-dose CBCT", poster presentation in 2009 *SPIE Medical Imaging conference*, Orlando, FL
2. **J. Wang**, T. Li, and L. Xing, "Low-dose CBCT Imaging for External Beam Radiotherapy", oral presentation in 2008 *ASTRO Annual Meeting*, Boston, MA
3. X. Zhang, **J. Wang**, L. Zhu, and L. Xing, "Low-dose X-ray fluoroscopy for Image Guided Radiation Therapy (IGRT)", poster presentation in 2008 *ASTRO Annual Meeting*, Boston, MA
4. **J. Wang**, T. Li, Z. Liang and L. Xing, "Dose reduction for kilovoltage cone-beam computed tomography in radiation therapy", oral presentation in 2008 *AAPM Annual Meeting*, (**selected for long presentation at the John S. Laughlin Science Council Research Symposium**), Houston, TX
5. **J. Wang,** L. Zhu**,** A. Chai, and L. Xing, "Temporal filtering of noise in low-dose x-ray fluoroscopy", poster presentation in 2008 *AAPM Annual Meeting*, Houston, TX
6. L. Zhu, **J. Wang**, Y. Xie, J. Starman, R. Fahrig, and L. Xing, "A patient set-up protocol based on partially blocked cone-beam CT", poster presentation in 2008 *AAPM Annual Meeting*, Houston, TX
7. **J. Wang**, T. Li, and L. Xing, "Iterative image reconstruction for on-board CBCT", poster presentation in 2008 *Electronic Portal Imaging & Positioning Devices*, San Francisco, CA

V. Conclusions

In summary, an infrastructure has been established to execute the proposed research. Novel image reconstruction and processing algorithms have been proposed for the treatment of prostate cancer. A few milestones have been achieved toward the general goal of the project. Implementation and evaluation of the image registration algorithms are current underway to

integrate the developed image reconstruction algorithms to improve the current prostate IMRT treatment.

VI. Reference:

1. L. Zhu, **J. Wang**, and L. Xing, "Noise suppression in scatter correction for Cone-Beam CT", *Medical Physics*, vol. 36, pp. 741-752, 2009
2. **J. Wang**, T. Li, Z. Liang and L. Xing, "Dose reduction for kilovoltage cone-beam computed tomography in radiation therapy", *Physics in Medicine and Biology*, vol. 53, pp. 2897-2909, 2008
3. **J. Wang**, A. Chai, L. Xing, "Noise correlation in CBCT projection data and its application for noise reduction in low-dose CBCT", poster presentation in 2009 *SPIE Medical Imaging conference*, Orlando, FL
4. **J. Wang**, T. Li, and L. Xing, "Low-dose CBCT Imaging for External Beam Radiotherapy", oral presentation in 2008 *ASTRO Annual Meeting*, Boston, MA
5. **J. Wang**, T. Li, and L. Xing, "Iterative image reconstruction for CBCT using edge-preserving prior", *Medical Physics*, vol. 36, pp. 252-260, 2009

VII. Appendices

Refereed publications in the last funding period

IOP PUBLISHING PHYSICS IN MEDICINE AND BIOLOGY

Phys. Med. Biol. **53** (2008) 2897–2909 doi:10.1088/0031-9155/53/11/009

Dose reduction for kilovotage cone-beam computed tomography in radiation therapy

Jing Wang[1], Tianfang Li[2], Zhengrong Liang[3] and Lei Xing[1]

[1] Department of Radiation Oncology, Stanford University School of Medicine, Clinical Cancer Center, 875 Blake Wilbur Drive, Rm CC-G204, Stanford, CA 94305-5847, USA
[2] Department of Radiation Oncology, University of Pittsburg Medical Center, Pittsburg, PA 15901, USA
[3] Department of Radiology, State University of New York, Stony Brook, NY 11794, USA

E-mail: lei@reyes.stanford.edu

Received 19 December 2007, in final form 12 March 2008
Published 6 May 2008
Online at stacks.iop.org/PMB/53/2897

Abstract

Kilovotage cone-beam computed tomography (kV-CBCT) has shown potentials to improve the accuracy of a patient setup in radiotherapy. However, daily and repeated use of CBCT will deliver high extra radiation doses to patients. One way to reduce the patient dose is to lower mAs when acquiring projection data. This, however, degrades the quality of low mAs CBCT images dramatically due to excessive noises. In this work, we aim to improve the CBCT image quality from low mAs scans. Based on the measured noise properties of the sinogram, a penalized weighted least-squares (PWLS) objective function was constructed, and the ideal sinogram was then estimated by minimizing the PWLS objection function. To preserve edge information in the projection data, an anisotropic penalty term was designed using the intensity difference between neighboring pixels. The effectiveness of the presented algorithm was demonstrated by two experimental phantom studies. Noise in the reconstructed CBCT image acquired with a low mAs protocol was greatly suppressed after the proposed sinogram domain image processing, without noticeable sacrifice of the spatial resolution.

(Some figures in this article are in colour only in the electronic version)

1. Introduction

Integration of the kilovotage cone-beam computed tomography (kV-CBCT) with a linear accelerator makes it possible to acquire a high-resolution volumetric image of a patient at a treatment position. There is growing interest in using on-board kV-CBCT for a patient treatment position setup and dose reconstruction in radiotherapy (Xing *et al* 2006, Yang *et al* 2007, Lee *et al* 2008). However, the repeated use of kV-CBCT during the course of a treatment

has raised concerns of an extra radiation dose delivered to patients (Brenner and Hall 2007, Islam *et al* 2006, Wen *et al* 2007). It has been reported (Wen *et al* 2007) that the dose delivered from Varian's kV-CBCT system with current clinical protocols is more than 3 cGy for central tissue and about 5 cGy for most of the peripheral tissues during an IMRT (intensity-modulated radiation therapy) treatment course for prostate cancer. The extra radiation exposure to normal tissue during kV-CBCT will significantly increase the probability of stochastic risk of inducing cancer and genetic defects. Based on the ALARA (as low as reasonably achievable) principle, the unwanted kV-CBCT dose should be minimized to fully realize its advantages of precise target localization during radiotherapy (Murphy *et al* 2007).

One way to reduce the radiation dose delivered to patients during the kV-CBCT procedure is to acquire CT projection data with a lower mAs level (can be realized by reducing the tube current or pulse time). However, the image quality of the projection image and the reconstructed CBCT image will be degraded due to excessive quantum noise as a result of a low mAs protocol. Conventionally, noise in CT is suppressed by using a low-pass filter to attenuate the high-frequency component of the projection data during reconstruction. The high-frequency component contains information of both noise and edges, where a simple low-pass filter cannot differentiate edge information from noise. Therefore, noise reduction using a low-pass filter will result in loss of edges, which is not desirable for CT imaging. Several edge-preserving filters (Hsieh 1998, Kachelriess *et al* 2001, Zhong *et al* 2004) have been proposed to reduce noise in CT images based on local characteristics of the projection data elements. More recently, statistics-based image domain (Li *et al* 2005a) and sinogram domain restoration algorithms (Li *et al* 2004, La Riviere 2005, La Riviere and Billmire 2005, Wang *et al* 2006) have shown advantages in noise reduction and edge preservation for low-dose fan-beam CT. In the meantime, noise properties of CT projection data have been under investigation (Li *et al* 2004, Whiting *et al* 2006) and the noise model of the sinogram data in Radon space (i.e. line integrals) has been validated by experimental studies (Wang *et al* 2008). In this work, we aim to improve the low-dose CBCT image quality by reducing noise in the CBCT sinogram before image reconstruction. The noise reduction algorithm incorporates the noise modeling of the CT sinogram data in Radon space (line integrals) to construct a penalized weighted least-squares (PWLS) objective function (Fessler 1994, Sukovic and Clinthorne 2000). The ideal solution of the line integrals is then estimated by minimizing the PWLS objective function. The weighted least square is based on the first and second moments of the noise in the sinogram data and an anisotropic penalty is designed to preserve the edges in the sinogram. CBCT images are reconstructed by using the Feldkamp–Davis–Kress (FDK) (Feldkamp *et al* 1984) algorithm after all sinogram images are processed by the PWLS criterion sequentially. The effectiveness of the PWLS-based noise reduction algorithm is demonstrated by two experimental phantom studies.

2. Methods and materials

2.1. CBCT sinogram smoothing

Ideally, the line integral of attenuation coefficients can be calculated by

$$p_i = \ln \frac{N_{i0}}{N_i}, \tag{1}$$

where N_{i0} and N_i are the incident photon number and detected photon number at the detector bin i respectively. For ease of presentation, we refer the measurement as a photon number. In a real x-ray CBCT system, the measured signal is total energy deposit on the flat-panel detector.

In the following of this paper, we refer the value of p_i as the sinogram datum at the detector bin i. Mathematically, the PWLS cost function in the sinogram domain can be written as

$$\Phi(p) = (\hat{y} - \hat{p})^T \Sigma^{-1} (\hat{y} - \hat{p}) + \beta R(p). \tag{2}$$

The first term in equation (2) is a weighted least-squares criterion, where $\hat{y}$ is the vector of the measured sinogram data and $\hat{p}$ is the vector of the ideal sinogram data to be estimated. The symbol T denotes the transpose operator. The matrix Σ is a diagonal matrix and its ith element is the variance of sinogram data at the detector bin i. The second term in equation (2) is a smoothness penalty or *a priori* constraint, where β is the smoothing parameter which controls the degree of agreement between the estimated and the measured data.

The element of the diagonal matrix Σ is the variance of the corresponding sinogram datum, and it determines the contribution of each sinogram datum to the cost function. Based on the sinogram noise modeling in Li *et al* (2004) and Wang *et al* (2008), the variance of the sinogram datum can be estimated by

$$\sigma_i^2 = \exp(p_i)/N_{i0}. \tag{3}$$

For a fixed incident photon number N_{i0}, a sinogram datum with a larger value will have a larger variance and therefore less contribution to the cost function since the weight of that measured datum is $1/\sigma_i^2$ as defined in equation (2). This can be understood by the following observation. A larger sinogram datum value p_i at the detector bin i indicates less x-ray photons being detected, i.e. smaller N_i in equation (1), or more photons being attenuated along the projection path i. A detector bin receiving less photons will be associated with a smaller signal-to-noise ratio (SNR) based on the Poisson noise nature of the detected x-ray photons. Therefore, the weighted least-squares criterion reflects the above observation that the measured datum with a lower SNR will contribute less for estimation of its ideal sinogram datum.

To calculate the sinogram datum variance at the detector bin i via equation (3), we need to estimate the incident photon number N_{i0} for calculation of the sinogram variance. The incident photon number is mainly determined by the protocols of tube current and the duration of x-ray pulse (i.e. mAs). Ideally, the incident x-ray flux from the tube would be calibrated as uniform as possible across a field of view (FOV), i.e. N_{i0} is a constant for all the detector bins. In reality, the x-ray flux is modulated to consider the concavity shape of the human body by the bow-tie attenuating filter prior to arrival at the patients. Therefore, the incident photon number will not be a constant across the FOV. To estimate the incident intensity over the FOV at a specific mAs level, we performed the air scan and then averaged the projection image over all projection view angles. Figure 1 shows the incident x-ray intensity with the tube current 80 mA and duration of pulse 10 ms. The incident x-ray intensity can then be used for estimation of the sinogram data variance $\{\sigma_i^2\}$.

The penalty term in equation (2) is a prior or smoothing constraint, which encourages the equivalence between neighboring data elements. In Li *et al* (2004) and Wang *et al* (2006), a penalty of a quadratic form with equal weights for all neighbors has been used for sinogram smoothing of fan-beam CT:

$$R(p) = \sum_n w_{in}(p_i - p_n)^2, \tag{4}$$

where n represents four nearest neighbors around pixel i and w_{in} is the weight for neighbor n. With an equal weight for the four nearest neighbors, these neighbors play an equivalent role in constraining the solution. As such, it provides a uniform regularization without considering details of intensity variation and possibly the presence of edges in the sinogram image. To preserve the edge information in the sinogram image of CBCT, we propose to use

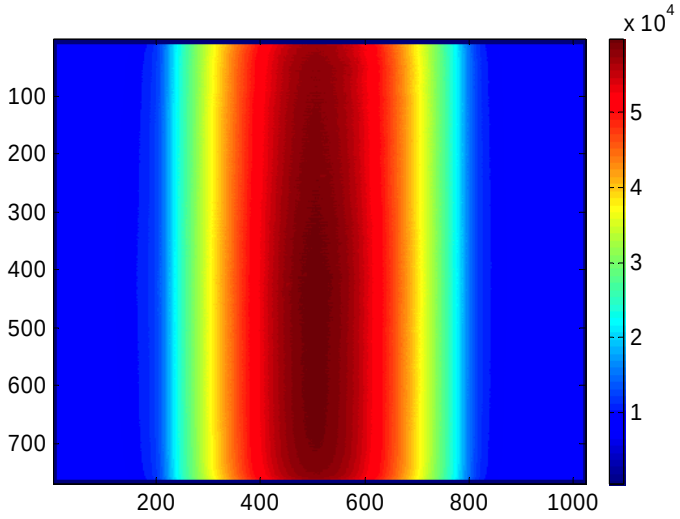

Figure 1. Incident x-ray intensities across the field of view with 80 mA tube current and 10 ms pulse time. Relative intensity is mainly caused by the bow-tie filter.

anisotropic weights for different neighbors in the sinogram image. The weight of the neighbor is determined by the magnitude of difference between neighbors and the concerned pixel. For a larger difference between the neighbor and the pixel, the coupling between them should be weaker and the weight w_{in} should be smaller. This form of weight is chosen the same as the conducting coefficient in the well-known anisotropic diffusion filter (Perona and Malik 1990):

$$w_{in} = \exp\left[-\left(\frac{p_i - p_n}{\delta}\right)^2\right], \tag{5}$$

where the gradient determines the strength of the diffusion during each iteration and the parameter δ was chosen as 90% of histogram of the gradient magnitude of the sinogram to be processed (Perona and Malik 1990).

Minimization of the objective function 2 can be performed efficiently by the iterative Gauss–Seidel updating strategy. The updating formula for the solution of $\hat{p}$ is given by

$$p_i^{(k+1)} = \frac{y_i + \beta\sigma_i^2\left(\sum_{n\in N_i^1} w_{in}\, p_n^{(k+1)} + \sum_{n\in N_i^2} w_{in}\, p_n^{(k)}\right)}{1 + \beta\sigma_i^2 \sum\limits_{n\in N_i} w_{in}}, \tag{6}$$

where the index k represents the iterative number, N_i^1 denotes those two nearest neighbors of i whose index is smaller than i, N_i^2 denotes those two nearest neighbors of i whose index is larger than i and $N_i$denotes these four nearest neighbors of pixel i in the sinogram image. The initial of $\hat{p}$ is given by the measured data $\hat{y}$.

2.2. On-board kV-CBCT

The cone-beam CT projection data were acquired by ExactArms (kV source/detector arms) of a Trilogy(tm) treatment system (Varian Medical Systems, Palo Alto, CA). The number of projections for a full 360° rotation is around 634. The dimension of each acquired projection image is 397 mm × 298 mm, containing 1024 × 768 pixels. The system has a FOV of 25 cm× 25 cm (full-fan mode) in the transverse plane and 17 cm in the longitudinal direction, which

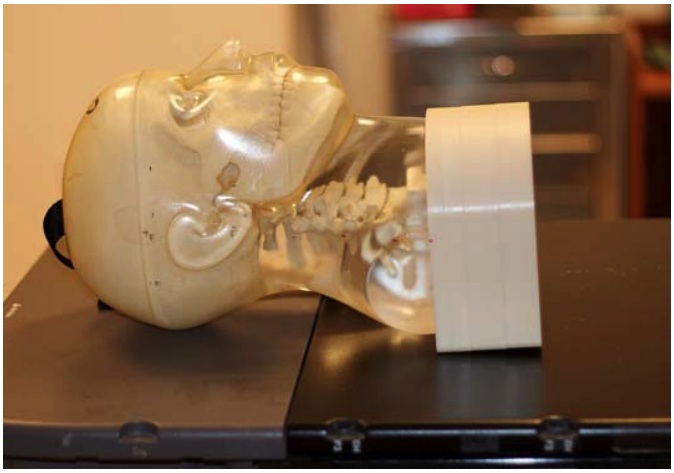

Figure 2. Illustration of the anthropomorphic head phantom used for evaluation of the PWLS algorithm.

can be increased to 45 cm × 45 cm in the transverse plane by shifting the detector laterally (half-fan mode).

Two phantoms were used to evaluate the performance of the proposed PWLS algorithm in this study. The first phantom is a commercial calibration phantom CatPhan® 600 (The Phantom Laboratory, Inc., Salem, NY). Details about the CatPhan® 600 phantom can be found in Li *et al* (2005a). The second one is an anthropomorphic head phantom (see figure 2). For each phantom, the x-ray tube current was set at 10 mA (low dose) and 80 mA (high dose) during acquisition of CBCT projection images. At both mA levels, the duration of the x-ray pulse at each projection view was 10 ms. The tube voltage was set to 125 kVp during all data acquisitions. After each sinogram acquired with the low-mAs protocol was processed by the PWLS algorithm described above, the CBCT image was reconstructed by the FDK algorithm. The voxel size in the reconstructed image is $0.5 \times 05 \times 0.5\ \text{mm}^3$.

3. Results

3.1. CatPhan® 600 phantom

We first tested the proposed algorithm on the CatPhan® 600 phantom. Several representative slices of the reconstructed CBCT are shown in figures 3, 4 and 6. In each of these figures, (a) is the FDK reconstructed image from the projection data acquired with 10 mA tube current, (b) is the FDK reconstructed image from the sinogram processed by the proposed PWLS sinogram smoothing algorithm and (c) is the FDK reconstructed image from the sinogram obtained with 80 mA tube current.

Figure 3 shows that one slice of image contains a point-like object, which mimics a fiducial marker. In figure 3(a), the point source is difficult to be observed. After the sinogram was processed by the PWLS algorithm, the reconstructed image (figure 3(b)) is very similar to that obtained with a high mA protocol (figure 3(c)). The point source was well recovered and easy to be detected.

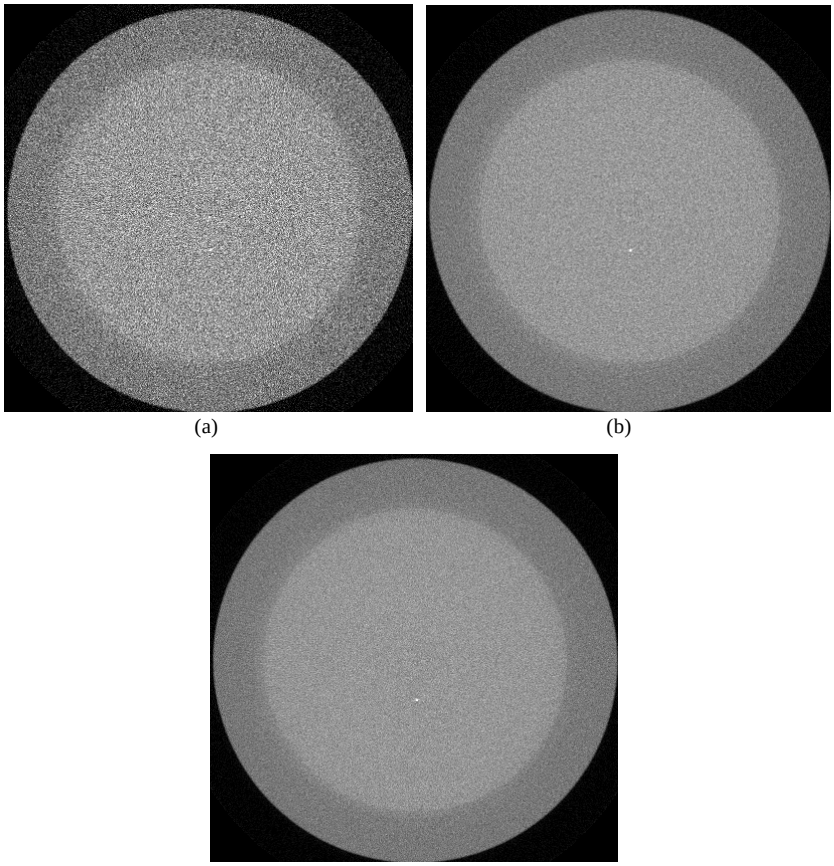

Figure 3. One slice of the FDK reconstructed image of the CatPhan® 600 phantom containing a point-like object: (a) from projection images acquired with 10 mA tube current, (b) after the sinogram acquired with 10 mA tube current is processed by the PWLS algorithm and (c) from projection images acquired with 80 mA tube current.

Figure 4 shows that one slice of image contains several strips with different sizes and contrasts, which can be used to study the edge information in the reconstructed images. The CT image reconstructed from the PWLS-processed sinogram is comparable to that obtained with the 80 mA protocol in terms of detectability of the strips; see ROI2 in figure 4(c). To show the difference between figures 4(a), (b) and (c), in figure 5 we plotted horizontal profiles along the central strips (see ROI1 in figure 4(c)). It can be observed that the edges are well preserved (compare profiles through figures 3(b) and (c)), while noise is effectively suppressed (compare profiles through figures 3(a) and (b)).

To further quantitatively evaluate the effectiveness of the PWLS sinogram smoothing algorithm, we calculated the contrast-to-noise ratio (CNR) at different regions of interest (ROIs) in the images shown in figure 6. The CNR is defined as

$$\mathrm{CNR} = \frac{|\mu_\mathrm{s} - \mu_\mathrm{b}|}{\sqrt{\sigma_\mathrm{s}^2 + \sigma_\mathrm{b}^2}}, \tag{7}$$

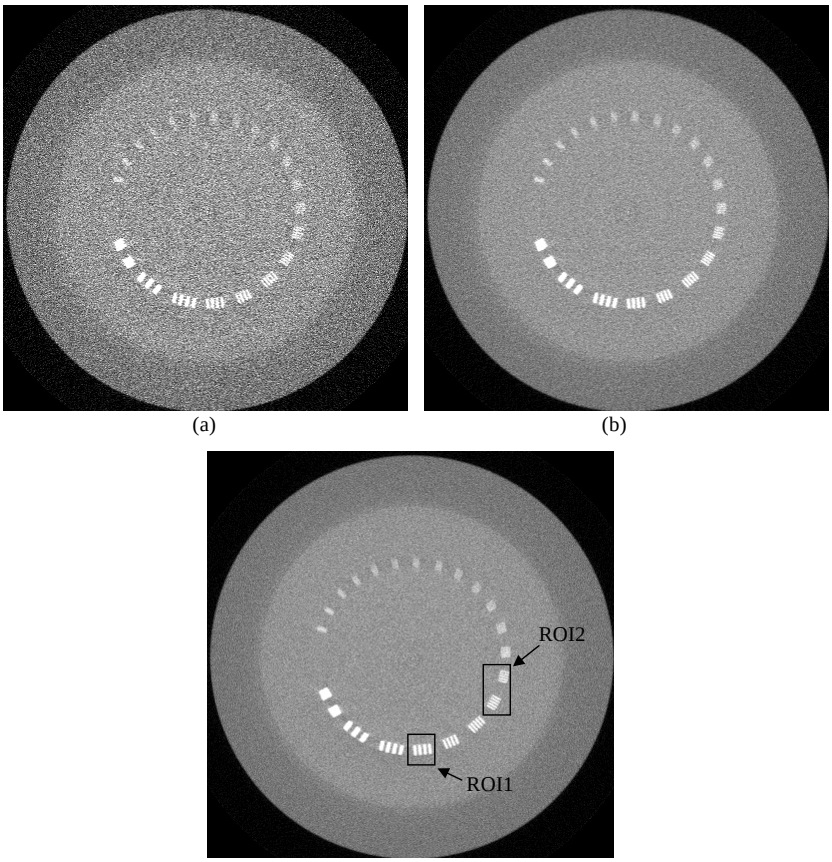

Figure 4. One slice of the FDK reconstructed image of the CatPhan® 600 phantom containing several strips: (a) from projection images acquired with 10 mA tube current, (b) after the sinogram acquired with 10 mA tube current is processed by the PWLS algorithm and (c) from projection images acquired with 80 mA tube current.

Table 1. CNRs of four ROIs in figure 5.

	ROI1	ROI2	ROI3	ROI4	ROI5
80 mA	1.83	7.31	4.75	1.51	0.89
10 mA	0.82	2.70	1.68	0.49	0.36
PWLS 10 mA $\beta = 0.05$	1.92	6.88	4.75	1.33	0.85

where μ_s is the mean value of the signal and μ_b is the mean value of the background. Five circular objects (indicated by arrows in figure 6) with different intensities were chosen to calculate CNRs. Table 1 lists the CNRs of these five ROIs. After a 10 mA sinogram was processed by the PWLS algorithm, the CNR in the reconstructed image improved significantly. It can be observed that the CNR of a PWLS-processed 10 mA image is comparable to that of the image acquired with the 80 mA protocol.

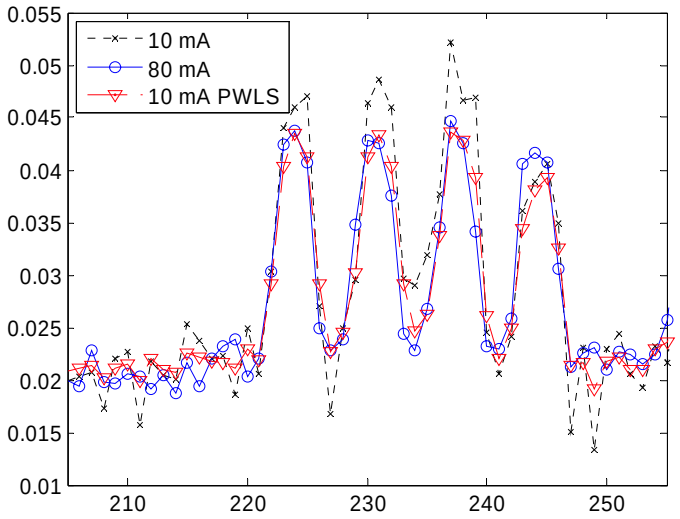

Figure 5. Profiles through the central strips in figure 4 (indicated by ROI1).

3.2. Anthropomorphic head phantom

Results of the anthropomorphic head phantom are shown in figure 7. Figure 7(a) shows one slice of the reconstructed images from projection data acquired with the 10 mA protocol. Figure 7(c) shows the reconstructed image from the PWLS-processed 10 mA sinogram. Figure 7(d) shows the same slice of the image reconstructed from the sinogram obtained with 80 mA. It can be observed that noise in 10 mA CT images is efficiently suppressed after the sinogram is processed by the PWLS algorithm. The processed low-dose CT (10 mA) image is very similar to its corresponding high-dose image (80 mA) by visual judgment. Standard deviation of the noise in a uniform ROI (as indicated by an arrow in figure 7(d)) is 2.8×10^{-3}in a low-dose (10 mA) image and 0.951×10^{-3} in its corresponding high-dose image. After the low-dose sinogram is processed by the PWLS algorithm with a smoothing parameter $\beta = 0.05$, the standard deviation of the same ROI is 0.955×10^{-3}, which is fairly close to the noise level of the 80 mA image.

To further illustrate how the edge information is affected by the PWLS sinogram smoothing, in figure 7(e) we show the difference image between figures 7(a) and (c). In the difference image, random noise is dominant and no edge or structure can be observed. This indicates that the edge information is well preserved in the PWLS-processed images.

4. Discussion

Generally, noise reduction for CT imaging can be performed in three spaces: projection data (either before or after logarithmic transform), filtered projection data (before backprojection operation during reconstruction) and reconstructed CT images. During filtering and backprojection operation, the noise properties will change significantly. Then noise modeling, such as distribution of noise and variance of noise, is difficult in filtered projection data and reconstructed image. Therefore, in this work we chose to work on the log-transformed data to fully utilize the noise model of the projection data in the Radon space (Li *et al* 2004, Wang *et al* 2008).

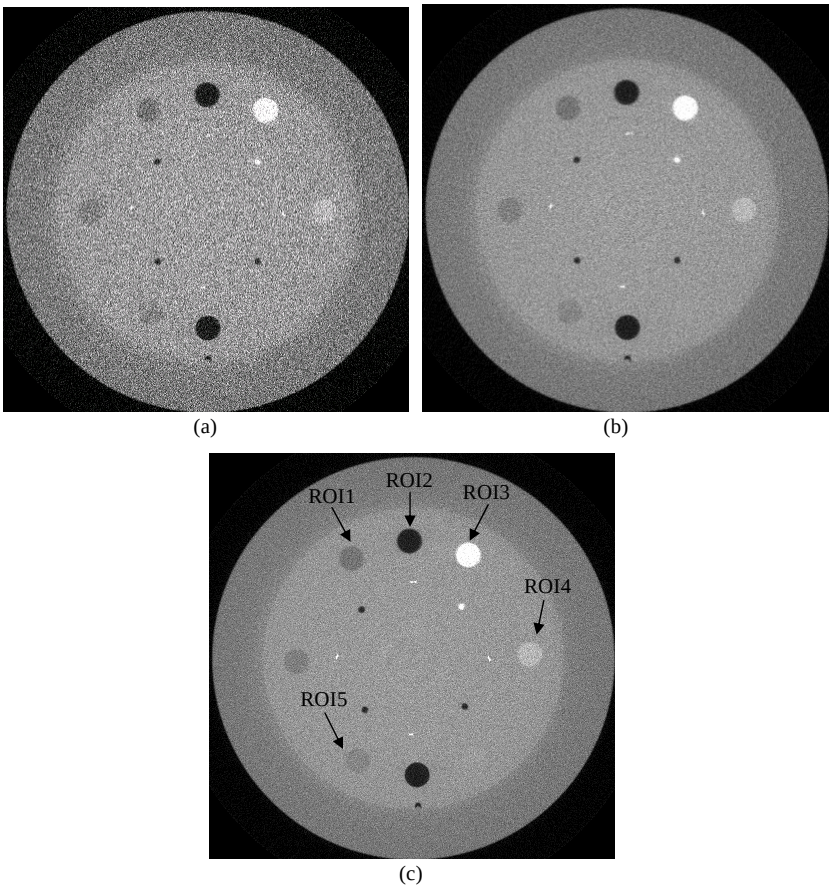

Figure 6. One slice of the FDK reconstructed image of the CatPhan® 600 phantom containing several circular objects with different intensities: (a) from projection images acquired with 10 mA tube current, (b) after the sinogram acquired with 10 mA tube current is processed by the PWLS algorithm and (c) from projection images acquired with 80 mA tube current.

Accurate noise modeling of measurement is fundamentally important in statistics-based image processing algorithms. Meanwhile, the regularization term also plays an important role in the performance of the algorithm. In CT sinogram processing, a commonly used regularization takes a quadratic form with equal weights for neighbors of an equal distance (La Riviere 2005, La Riviere and Billmire 2005, Li *et al* 2004, Wang *et al* 2006). Such a quadratic penalty simply encourages the equivalence between neighbors without considering discontinuities in the image and may lead to over-smoothing around sharp edges or boundaries. In the presented algorithm, we proposed an anisotropic penalty to consider the difference among neighbors. The idea was inspired by the well-known anisotropic diffusion filter (Perona and Malik 1990), in which the gradient controls the strength of diffusion among neighbors. The coupling between neighbors should be smaller if the absolute value of difference between them is smaller and this kind of neighbors should contribute less to the solution of the concerned pixel (see equation (6)). There are many choices that satisfy this behavior of weighting. In this work, the form of the anisotropic weight was chosen the same as the conduction coefficients

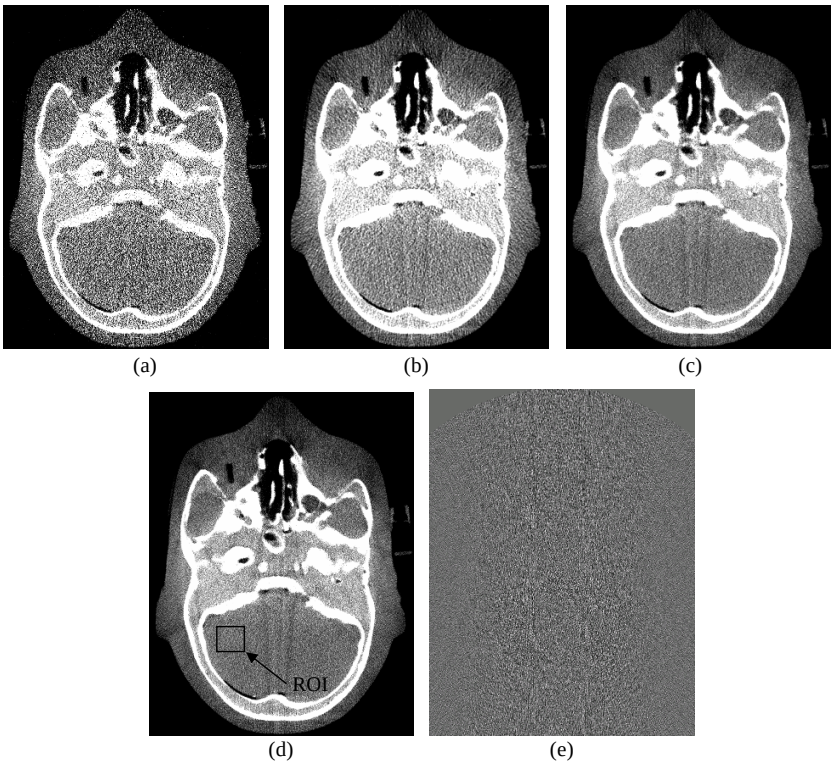

Figure 7. One slice of FDK reconstructed image of the anthropomorphic head phantom: (a) from projection images acquired with 10 mA tube current, (b) using a low-pass Hanning filter with cutoff 80% Nyquist frequency, (c) after the sinogram acquired with 10 mA tube current is processed by the PWLS algorithm, (d) from projection images acquired with 80 mA tube current and (e) difference image between (d) and (c).

in the anisotropic diffusion filter (Perona and Malik 1990). By such a choice, the anisotropic quadratic form penalty discourages the equivalence between neighbors if the gradient between them is large, and the edges or boundaries in the image will be better preserved. This effect is similar to that of anisotropic coefficients in the diffusion filter.

In the presented method, the reconstruction of CT images was performed by an analytical FDK algorithm for its speed and accuracy. During the FDK reconstruction process, noise can also be suppressed by using a low-pass filter. It has been reported (Li *et al* 2004, La Riviere 2005) that a statistics-based sinogram smoothing algorithm plus FBP reconstruction is superior to conventional low-pass filters for noise suppression of 2D fan-beam CT. In this work, we also reconstructed the CT image of the anthropomorphic head phantom using a Hanning filter with a cutoff at 80% Nyquist frequency, see figure 7(b). It can be observed that the image reconstructed from the PWLS-processed sinogram is superior to the result of the Hanning filter in terms of noise suppression and structure preservation.

Similar to the cutoff frequency in the conventional low-pass filter during reconstruction, there is also a free parameter β in the presented method which controls the trade-off of the noise level and the structure preservation in reconstructed images. In this work, the choice of β is determined by the visual judgment. The optimal choice of the parameter β can be determined by more sophisticated ways such as the received operating characteristic (ROC)

study. Nevertheless, the parameter β can be chosen according to the noise level of the sinogram because from equation (6),the solution for the ideal sinogram, we can see that the parameter β and variance σ_i^2 are always coupled together. The noise level of the projection data is mainly determined by two factors: incident photon number and line integrals. As such, the parameter β could be optimized at a certain mAs level and treatment site for patients of a similar size. In this work, however, the parameter is chosen empirically, which is justifiable when the dependence of the parameter on the noise level is weak.

The method presented in this paper is based on the noise properties of the sinogram, and the smoothing constraint or penalty is applied to the sinogram domain. Based on the same noise model, the smoothing constraint can also be applied to the CT image domain, and the statistical iterative reconstruction (SIR) algorithm can be used to obtain the attenuation coefficient map by minimizing the objective function. The SIR-based algorithms showed some advantages over the conventional filtered backprojection method for multi-slice helical CT (Thibault *et al* 2007). However, an obstacle for practical use of SIR is the computation burden, especially for large volume datasets of CBCT. It takes more than 10 h to reconstruct the typical volume of multi-slice helical CT using SIR (Thibault *et al* 2007). It takes only 3 s for the presented sinogram smoothing method to process one projection image using a PC with 3.0 GHz CPU. Parallel computing can speed up both SIR and sinogram-based algorithms significantly using the cell broadband engine (Knaup *et al* 2006) and PC cluster (Li *et al* 2005b). It is possible to achieve clinically acceptable time for the presented sinogram smoothing algorithm through parallel computation. It is an interesting research topic to quantitatively compare the performance of the SIR-based CBCT reconstruction algorithm and the statistics-based sinogram smoothing method.

When CBCT is used for patient setup and target localization during radiotherapy, some extra information may be taken into account for dose and noise reduction. For example, a complete CT volume dataset with high clarity used for treatment planning is usually available before the treatment. This will provide strong *a priori* information of the patient before each CBCT scan. Prior information of planning 3D CT has been proved useful to improve the image quality of 4D CBCT (Li *et al* 2007). It is expected that the radiation dose of CBCT used for radiotherapy can be further reduced by incorporating the planning CT information into the image restoration or reconstruction algorithms.

In the report of the AAPM task group 75 (Murphy *et al* 2007), several dose reduction strategies for image-guided radiotherapy were discussed. For CBCT, dose reduction can be achieved by narrowing field of view to avoid delivering radiation to an unnecessary region of the patient (Murphy *et al* 2007). Compared with these hardware-based approaches, software approaches (such as the one proposed in this paper) provide a more cost-effective means for dose reduction of CBCT. In addition to the statistics-based reconstruction and restoration algorithms, advanced analytical CBCT reconstruction algorithms (Leng *et al* 2007, Zhuang *et al* 2006, Zou and Pan 2004, Zou *et al* 2005) may further improve the low-dose CBCT image quality.

5. Conclusion

A PWLS algorithm with non-uniform weights was proposed to reduce noise in low-dose onboard CBCT. In this method, the sinogram was first processed according to the PWLS criterion. The weight for each measurement was chosen as sinogram datum variance, where variance can be estimated accurately according to the sinogram noise model. To preserve edge information during noise reduction, we proposed an anisotropic quadratic form penalty. The quadratic form penalty encourages equivalence between neighbors and the anisotropic

penalty provides the mechanism to control the influence of different neighbors according to its corresponding gradient. The effectiveness of the proposed method is demonstrated by two experimental phantom studies. The quality of the 10 mA CT image after its sinogram processed by the PWLS algorithm is comparable to the image obtained with the 80 mA protocol. These experimental results indicate that it is possible to reduce the CBCT radiation dose by a factor of 1/8 without loss of useful information for radiotherapy.

Acknowledgment

This work was supported in part by grants from the Department of Defense (PC040282 and PC073592) and National Cancer Institute (1R01 CA98523 and CA104205). Dr Liang was supported by the National Cancer Institute under grants CA082402 and CA120917.

References

Brenner D and Hall E 2007 Current concepts—computed tomography—an increasing source of radiation exposure *New Engl. J. Med.* **357** 2277–84

Feldkamp L, Davis L and Kress J 1984 Practical cone-beam algorithm *J. Opt. Soc. Am.* A **1** 612–9

Fessler J 1994 Penalized weighted least-squares image-reconstruction for positron emission tomography *IEEE Trans. Med. Imaging* **13** 290–300

Hsieh J 1998 Adaptive streak artifact reduction in computed tomography resulting from excessive x-ray photon noise *Med. Phys.* **25** 2139–47

Islam M, Purdie T, Norrlinger B, Alasti H, Moseley D, Sharpe M, Siewerdsen J and Jaffray D 2006 Patient dose from kilovoltage cone beam computed tomography imaging in radiation therapy *Med. Phys.* **33** 1573–82

Kachelriess M, Watzke O and Kalender W 2001 Generalized multi-dimensional adaptive filtering for conventional and spiral single-slice, multi-slice, and cone-beam CT *Med. Phys.* **28** 475–90

Knaup M, Kalender W A and Kachelrieb M 2006 Statistical cone-beam CT image reconstruction using the cell broadband engine *IEEE Nucl. Sci. Symp. Conf. Record* **5** 2837–40

La Riviere P 2005 Penalized-likelihood sinogram smoothing for low-dose CT *Med. Phys.* **32** 1676–83

La Riviere P and Billmire D 2005 Reduction of noise-induced streak artifacts in X-ray computed tomography through spline-based penalized-likelihood sinogram smoothing *IEEE Trans Med. Imaging* **24** 105–11

Lee L, Le Q and Xing L 2008 Retrospective IMRT dose reconstruction based on cone-beam CT and MLC log-file *Int. J. Radiat. Oncol. Biol. Phys.* **70** 634–44

Leng S, Zhuang T, Nett B and Chen G 2007 Helical cone-beam computed tomography image reconstruction algorithm for a tilted gantry with N-PI data acquisition *Opt. Eng.* **46** 15004

Li T, Koong A and Xing L 2007 Enhanced 4D cone-beam CT with inter-phase motion model *Med. Phys.* **34** 3688–95

Li T, Li X, Wang J, Wen J, Lu H, Hsieh J and Liang Z 2004 Nonlinear sinogram smoothing for low-dose X-ray CT *IEEE Trans. Nucl. Sci.* **51** 2505–13

Li T, Schreibmann E, Thorndyke B, Tillman G, Boyer A, Koong A, Goodman K and Xing L 2005a Radiation dose reduction in four-dimensional computed tomography *Med. Phys.* **32** 3650–60

Li X, Ni J and Wang G 2005b Parallel iterative cone-beam CT image reconstruction on a PC cluster *J. X-Ray Sci. Tech.* **13** 63–72

Murphy M *et al* 2007 The management of imaging dose during image-guided radiotherapy: report of the AAPM Task Group 75 *Med. Phys.* **34** 4041–63

Perona P and Malik J 1990 Scale-space and edge-detection using anisotropic diffusion *IEEE Trans. Pattern Anal.* **12** 629–39

Sukovic P and Clinthorne N 2000 Penalized weighted least-squares image reconstruction for dual energy X-ray transmission tomography *IEEE Trans. Med. Imaging* **19** 1075–81

Thibault J B, Sauer K D, Bouman C A and Hsieh J 2007 A three-dimensional statistical approach to improved image quality for multislice helical CT *Med. Phys.* **34** 4526–44

Wang J, Li T, Lu H and Liang Z 2006 Penalized weighted least-squares approach to sinogram noise reduction and image reconstruction for low-dose X-ray computed tomography *IEEE Trans. Med. Imaging* **25** 1272–83

Wang J, Lu H, Eremina D, Zhang G, Zhang G, Wang S, Chen J, Manzione J and Liang Z 2008 An experimental study on the noise properties of X-ray CT sinogram data in the Radon space *Proc. SPIE Med. Imaging* **6913** 69131M

Wen N, Guan H, Hammoud R, Pradhan D, Nurushev T, Li S and Movsas B 2007 Dose delivered from Varian's CBCT to patients receiving IMRT for prostate cancer *Phys. Med. Biol.* **52** 2267–76

Whiting B, Massoumzadeh P, Earl O, O'Sullivan J, Snyder D and Williamson J 2006 Properties of preprocessed sinogram data in x-ray computed tomography *Med. Phys.* **33** 3290–303

Xing L, Thorndyke B, Schreibmann E, Yang Y, Li T F, Kim G Y, Luxton G and Koong A 2006 Overview of image-guided radiation therapy *Med. Dosim.* **31** 91–112

Yang Y, Schreibmann E, Li T, Wang C and Xing L 2007 Evaluation of on-board kV cone beam CT (CBCT) based dose calculation *Phys. Med. Biol.* **52** 685–705

Zhong J, Ning R and Conover D 2004 Image denoising based on multiscale singularity detection for cone beam CT breast imaging *IEEE Trans. Med Imaging* **23** 696–703

Zhuang T, Nett B, Leng S and Chen G 2006 A shift-invariant filtered backprojection (FBP) cone-beam reconstruction algorithm for the source trajectory of two concentric circles using an equal weighting scheme *Phys. Med. Biol.* **51** 3189–210

Zou Y and Pan X 2004 Exact image reconstruction on PI-lines from minimum data in helical cone-beam CT *Phys. Med. Biol.* **49** 941–59

Zou Y, Pan X and Sidky E 2005 Theory and algorithms for image reconstruction on chords and within regions of interest *J. Opt. Soc. Am.* A **22** 2372–84

Iterative image reconstruction for CBCT using edge-preserving prior

Jing Wang
Department of Radiation Oncology, Stanford University School of Medicine, Stanford, California 94305

Tianfang Li
Department of Radiation Oncology, University of Pittsburgh Cancer Institute, Pittsburgh, Pennsylvania 15901

Lei Xing[a)]
Department of Radiation Oncology, Stanford University School of Medicine, Stanford, California 94305

(Received 8 March 2008; revised 5 November 2008; accepted for publication 5 November 2008; published 29 December 2008)

On-board cone-beam computed tomography (CBCT) is a new imaging technique for radiation therapy guidance, which provides volumetric information of a patient at treatment position. CBCT improves the setup accuracy and may be used for dose reconstruction. However, there is great concern that the repeated use of CBCT during a treatment course delivers too much of an extra dose to the patient. To reduce the CBCT dose, one needs to lower the total mAs of the x-ray tube current, which usually leads to reduced image quality. Our goal of this work is to develop an effective method that enables one to achieve a clinically acceptable CBCT image with as low as possible mAs without compromising quality. An iterative image reconstruction algorithm based on a penalized weighted least-squares (PWLS) principle was developed for this purpose. To preserve edges in the reconstructed images, we designed an anisotropic penalty term of a quadratic form. The algorithm was evaluated with a CT quality assurance phantom and an anthropomorphic head phantom. Compared with conventional isotropic penalty, the PWLS image reconstruction algorithm with anisotropic penalty shows better resolution preservation. [DOI: 10.1118/1.3036112]

Key words: cone-beam CT, low-dose, iterative reconstruction, PWLS, edge-preserving penalty

I. INTRODUCTION

Integration of the cone-beam computed tomography (CBCT) with a linear accelerator[1] makes it possible to acquire volumetric image of high spatial resolution for a patient at treatment position. There is growing interest in using on-board CBCT for patient setup and dose reconstruction.[2] Repeated use of CBCT during a treatment course has raised concern of the extra radiation dose delivered to patients.[3,4] One cost-effective way to reduce the CBCT dose is to acquire CT with a lower mAs protocol. However, image quality will degrade dramatically due to excessive noise,[5,6] rendering the low-mAs CBCT a less attractive option for the therapeutic guidance.

In this work, we incorporate the noise properties of CBCT log-transformed projection data[7,8] in a statistical iterative image reconstruction algorithm to improve the low-dose CBCT image quality. Compared with analytical reconstruction algorithms, a major advantage of iterative algorithms is that it takes into consideration the image physics, noise properties, and imaging geometry elegantly. Advantages of iterative reconstruction algorithms have been demonstrated in the image reconstruction of emission tomographic images.[9–12] However, when applying iterative reconstruction algorithms for CT imaging,[13–17] long computational time may pose a challenge for their clinical applications. With the development of fast computers and dedicated hardwares,[18,19] iterative reconstruction algorithms may be used for clinical CT reconstruction in the near future. Recently, iterative image reconstruction algorithms have demonstrated superior performance for reconstruction of the multislice helical CT (Ref. 20) and cardiac micro-CT.[21] Prototype products based on iterative reconstruction methods have been exhibited by major CT vendors in a number of national and international meetings.

In statistics-based iterative reconstruction algorithms, tomographic images are reconstructed by minimizing or maximizing a cost function, which is constructed based on noise characteristics of the measured data. There are usually two terms in the objective function. The first term models the statistics of measured data and the second term reflects *a prior* information to regularize the solution. Many efforts[7,22] have been devoted to investigate the noise models of the measurements in CT. Accurate noise modeling is a prerequisite of a statistical iterative reconstruction algorithm. The second term, i.e., the regularization term, also plays an important role for successful image reconstruction. One common choice of the regularization term is the Gaussian Markov random field in quadratic form.[16,23–25] Such quadratic penalty with equal weights for neighbors of equal distance encourages equivalence between neighbors without considering discontinuities in images, which may lead to oversmoothing around edges or boundaries. Several edge-preserving regularization methods have been proposed to address this problem. For example, the edge-preserving Huber penalty, which penalizes neighbors of small differences quadratically while applying a linear penalty on neighbors of

larger difference, has been used by Elbakri and Fessler[26] for CT image reconstruction and by Chlewicki *et al.*[27] for positron emission tomography reconstruction. A line process has been introduced by Geman and Geman[28] to define the edge lattice during Bayesian restoration of images. Geman and Reynolds[29] proposed a finite asymptotic edge-preserving function and Charbonnier *et al.*[30] introduced an auxiliary variable in the prior constraint to mark the discontinuities in the images. These modifications make the objective function nonquadratic and complicate the computation. In this work, we propose a quadratic regularization term with anisotropic weights for different neighbors. The role of the anisotropic penalty is to discourage the equivalence between neighbors if the gradient is large; thus the edges or discontinuities will be better preserved in the final reconstructed image.

In the following sections, we first introduce the penalized weighted least squares (PWLS) objective function for image reconstruction of CBCT based on the noise properties of CBCT projection data. We then describe the proposed anisotropic penalty in details. In Sec. III, the evaluation of the proposed algorithm is presented using a quality assurance phantom and an anthropomorphic head phantom, followed by the discussion in Sec. IV and the conclusion in Sec. V.

II. METHODS AND MATERIALS

II.A. PWLS image reconstruction

Noise in x-ray CT projection data after logarithm transform follows approximately Gaussian distribution and the variance of the noise can be determined by an exponential formula[7,8]

$$\sigma_i^2 = \exp(\overline{p_i})/N_{i0}, \tag{1}$$

where N_{i0} is the incident photon number at detector bin i, $\overline{p_i}$ and σ_i^2 is the mean and variance of projection datum p_i, respectively. Based on the noise properties of CT projection data, the PWLS cost function in the image domain can be written as

$$\Phi(\mu) = (\hat{p} - A\mu)'\Sigma^{-1}(\hat{p} - A\mu) + \beta R(\mu). \tag{2}$$

The first term in Eq. (2) is the weighted least-squares criterion, where $\hat{p}$ is the vector of log-transformed projection measurements, and μ is the vector of attenuation coefficients to be reconstructed. Operator A represents the system or projection matrix. The element of a_{ij} is the length of the intersection of projection ray i with pixel j and it is calculated by a fast ray-tracing technique.[31] In our implementation, the element of matrix A was precomputed, stored as a file, and used as a lookup table later. The projection data $\hat{p}$ and the attenuation map μ is related by $\hat{p}=A\mu$. Σ is a diagonal matrix with the ith element of σ_i^2, i.e., an estimate of the variance of measured $\hat{y}_i$ at detector bin i which can be estimated from the measured projection data according to Eq. (1). The element of the diagonal matrix plays the role of weighting in the WLS cost function and it determines contribution of each measurement. The symbol $'$ denotes the transpose operator. The second term in Eq. (2) is a smoothness penalty or a prior constraint, where β is the smoothing or penalty parameter which controls relative contribution from the measurement and prior constraint. The image reconstruction task is to find attenuation map μ by minimizing the objective function (2) with a positive constraint. The Gaussian–Seidel updating strategy was used for the minimization and details about the implementation are described in the Appendix.

II.B. Edge-preserving anisotropic penalty

The prior constraint in Eq. (2) enforces a roughness penalty on the solution. The quadratic penalty with equal weights for neighbors of the same distance has been used widely for iterative image reconstruction[16,17,23,25]

$$R(\mu) = \mu' R\mu = \frac{1}{2}\sum_j \sum_{m\in N_j} w_{jm}(\mu_j - \mu_m)^2, \tag{3}$$

where index j runs over all image elements in the image domain, N_j represents the set of neighbors of the jth image pixel. The parameter w_{jm} was set to 1 for first-order neighbors and $1/\sqrt{2}$ for second-order neighbors in previous applications.[17,23,25] This type of penalty only takes distance information of the neighbors into account. That is, the neighbors of the same distance play an equivalent role in regularizing the solution, and *vise versa*. A major shortcoming of the approach is that the regularization does not take the difference in intensities of the neighboring voxles (e.g., edges or discontinuities) into account, which may lead to an oversmoothed solution for reconstructed images. To overcome this limitation, we propose an anisotropic penalty to regularize the solution. In this formulation, the weight is smaller if the difference between a neighbor and the concerned voxel is larger, since the coupling between two such neighbors is smaller. There are many choices that satisfy this behavior of weighting. In this work, we chose the form of w_{jm} to be the same as the conduction coefficient in the well-known anisotropic diffusion filter.[32] The weight w_{jm} can be written as

$$w'_{jm} = w_{jm}\exp\left[-\left(\frac{\mu_j - \mu_m}{\delta}\right)^2\right], \tag{4}$$

where the gradient and the parameter δ determine the strength of the diffusion during each iteration. The parameter δ can be set either by hand or to the value at 90% of the histogram of the gradient magnitude of the image to be processed. In this work, we set the value of δ to be 90% of the histogram of the gradient magnitude of the FDK reconstructed image (which is used as the initial during iterative reconstruction).

II.C. CBCT data acquisition

Cone-beam CT projection data were acquired by an Acuity simulator (Varian Medical Systems, Palo Alto, CA). The number of projections for a full 360° rotation is 680 and the total time for the acquisition of one full circle of the projection data is about 1 min. The dimension of each acquired projection image is 397 mm $\times$ 298 mm, containing 1024 $\times$ 768 pixels. To save computational time during iterative reconstruction, the projection data at each projection view

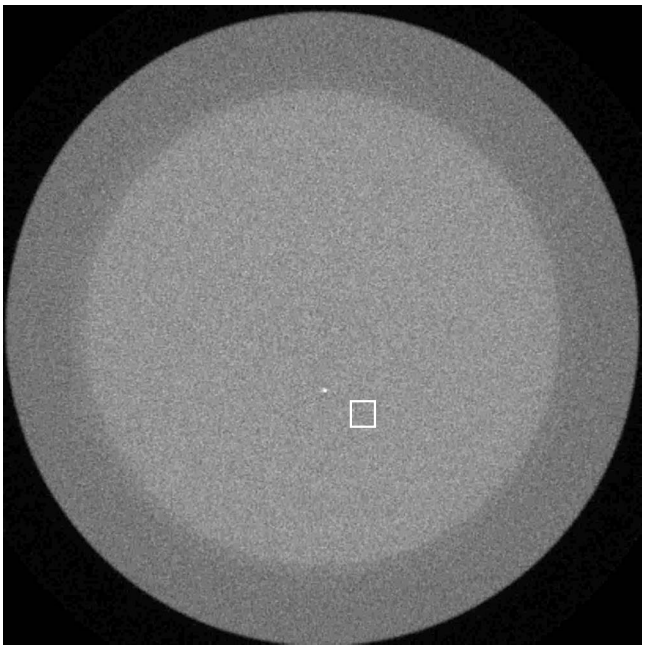

FIG. 1. The bead point object in the CatPhan® 600 phantom was used to calculate the MTF of reconstructed images. Display window: $[0,0.03]$ mm^{-1}. The white square in the image indicates the region used to calculate the standard deviation.

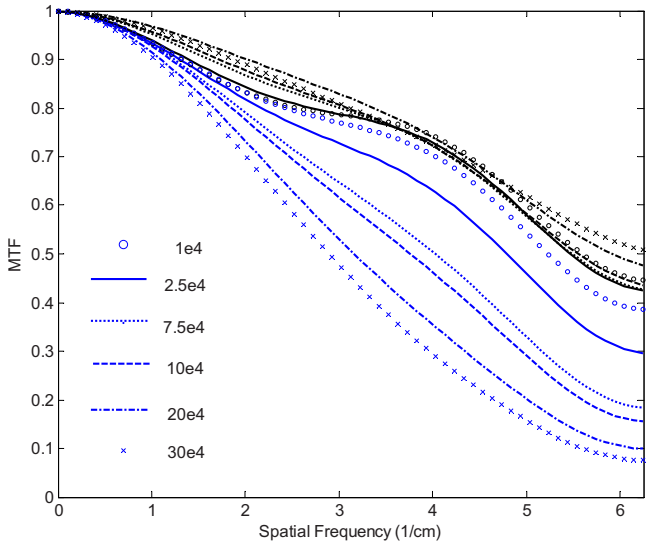

FIG. 2. MTF curves of two PWLS iterative image reconstruction algorithms with different smoothing parameters. Curves in the blue color are results of reconstruction using an isotropic quadratic penalty. Curves in the black color are results of reconstruction using the edge-preserving anisotropic quadratic penalty.

were downsampled by a factor of 2 and only 16 out of 768 projection data along the axial direction were chosen for reconstruction. The system has a field of view of 25 cm $\times$25 cm (full-fan mode) in the transverse plane and 17 cm in the longitudinal direction, which can be increased to 45 cm $\times$45 cm in the transverse plane by shifting the detector laterally (half-fan mode).

Two phantoms were used to evaluate the performance of the proposed PWLS algorithm. The first is a commercial calibration phantom CatPhan® 600 (The Phantom Laboratory, Inc., Salem, NY). The second is an anthropomorphic head phantom. In both phantom studies, the tube voltage was set to 125 kVp. The x-ray tube current was set at 10 mA and the duration of the x-ray pulse at each projection view was 10 ms during the acquisition of low-dose CBCT projection data. During acquisition of the corresponding high-dose CBCT image, the tube current was set at 80 mA and the duration of the x-ray pulse was set at 12 ms. The projection data were acquired in full-fan mode and the full-fan bow-tie filter was used for both phantoms. The distance of source-to-axis is 100 cm and source-to-detector distance of 150 cm. The size of reconstructed image is $350\times350\times16$ and voxel size is $0.776\times0.776\times0.776$ mm^3.

II.D. Performance evaluation

We used the CatPhan® 600 phantom to study the spatial resolution of images reconstructed by different algorithms. The CTP591 module of the CatPhan® 600 phantom contains a bead point object with a diameter of 0.28 mm (see Fig. 1). The point object can be used to calculate the modulation transfer function (MTF) which characterizes the spatial resolution of images. The reconstructed image contains the point object provides the point-spread-function for each reconstruction algorithm and the in-plane MTF can be obtained by calculating two-dimension Fourier transform and averaging over 2π angles. A 10×10 matrix centered about the point object was used to calculate the MTF after the background value (which can be estimated by averaging the values of a uniform background region) was subtracted from the value of each pixel.

In the CTP404 module of the CatPhan® 600, there are several circles of different intensities which can be used to quantify the contrast-to-noise (CNR) of the reconstructed images in different reconstructions. We selected a low-contrast region of interest (ROI) for calculation of the CNR in the image reconstructed by different algorithms since a low-contrast region is of interest in CT imaging. The contrast was calculated as the absolute difference between the mean value of the region inside the ROI and the mean value of the uniform background region. The noise level was characterized by the standard deviation of a uniform area of size 15 pixels by 15 pixels. The CNR was defined as the contrast divided by the standard deviation.

III. RESULTS

III.A. CatPhan® 600 phantom

III.A.1. MTF measurement

Figure 2 shows the MTFs of two iterative reconstruction algorithms with different smoothing parameters β ranging from 1.0×10^4 to 30×10^4. It can be observed that the spatial resolution of the reconstructed image using an isotropic quadratic penalty decreases as smoothing strength increases. The frequency of 50% MTF for the iterative reconstruction using the isotropic penalty decreases from 5.25 to 2.91 1/cm as

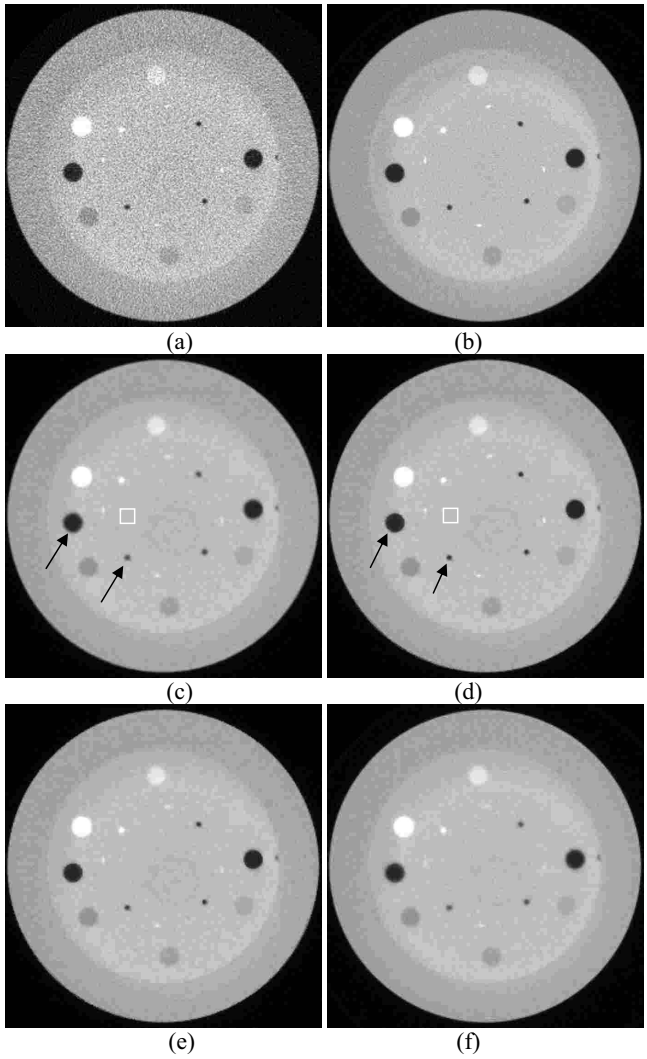

FIG. 3. CBCT of the CatPhan® 600 phantom: (a) analytical FDK reconstructed image from projection data acquired using a low-dose protocol (10 mA/10 ms) and (b) a high-dose protocol (80 mA/12 ms); (c) PWLS iterative image reconstruction with the isotropic quadratic penalty from projection data acquired using a low-dose protocol and (d) with the proposed anisotropic penalty; (e) PWLS iterative image reconstruction with the Huber penalty; (f) analytical FDK reconstructed image after low-dose projection data processed by the PWLS criterion (Ref. 34) with a smoothing parameter of 0.09. Display window: $[0,0.02]$ mm^{-1}.

the smoothing parameter increases from 1.0×10^4 to 30×10^4. In contrast, MTF curves of the image reconstructed using the proposed edge-preserving anisotropic quadratic penalty are clustered together with various smoothing parameters. This indicates that the spatial resolution in images reconstructed using the anisotropic quadratic penalty is better-preserved.

III.A.2. Full width at half maximum measurement

We then tested the proposed algorithm on the CTP404 module of the CatPhan® 600 phantom. A representative slice of the CBCT images obtained by different reconstruction methods are shown in Fig. 3. Figure 3(a) is the low-dose image reconstructed by analytical FDK algorithm. It can be observed that noise level is high in this low-dose CBCT image. Figure 3(c) shows the image reconstructed by the PWLS algorithm using the isotropic quadratic penalty with the penalty parameter $\beta=30\times10^4$. Figure 3(d) displays the image reconstructed by the PWLS algorithm using the proposed edge-preserving anisotropic penalty with the same penalty parameter. The noise in the images reconstructed by iterative algorithms is greatly suppressed compared with the image reconstructed using the analytical method. It is seen that the edges were blurred in Fig. 3(c), as indicated by the arrows in the image. This is not surprising since an isotropic quadratic form penalty simply encourages equivalence among neighbors along all directions without considering the boundary information presented in the image. However, edges were well preserved when the anisotropic penalty was used as the constraint (see the corresponding area in Fig. 3(d) indicated by the arrows).

To quantitatively analyze the gain by using the anisotropic penalty in the iterative reconstruction algorithm, we then studied the full-width-at-half-maximum (FWHM) of two pointlike objects (one is brighter than background and the other one is darker than the background) in the reconstructed images. Figure 4 shows the profiles passing through two pointlike objects in Figs. 3(c) and 3(d). Through those profiles, it can be observed that the major difference between the solutions using isotropic and anisotropic penalties is nearby edges. The intensity values in both images at a uniform region are nearly identical; see line along value 0.016 in both Figs. 4(a) and 4(b). It can also be observed in Fig. 4 that the peak of the profile from the image reconstructed using the isotropic quadratic penalty is lower than that from the reconstructed image using the anisotropic penalty, while the bottom of the profile from the image reconstructed using the isotropic quadratic penalty is higher than that from the reconstructed image using anisotropic penalty. These observations show that there is a signal loss when an image is reconstructed by the PWLS algorithm using the isotropic penalty. The standard deviation of a uniform region (indicated by a white square) is 0.50×10^{-3} in Fig. 3(c) and 0.54×10^{-3} in Fig. 3(d). We then fitted the profile to a Gaussian functional. The FWHM of brighter source is 3.48 pixels for the image reconstructed with the isotropic penalty and 3.19 pixels for the anisotropic penalty. The FWHM for the darker source is 3.71 pixels for the image reconstructed with the isotropic penalty and 3.48 pixels for the anisotropic penalty. In both cases, better edge preserving was observed in the image reconstructed using the anisotropic penalty.

III.A.3. CNR measurement

Table I lists the CNR of two iterative reconstruction algorithms with different smoothing parameters. It can be observed that in both reconstruction algorithms the CNR increase as smoothing parameter increases. The CNR of the image reconstructed using the anisotropic penalty is slightly larger than that of the isotropic penalty when the same smoothing parameters are used. However, at the matched resolution between the two methods, CNR was increased

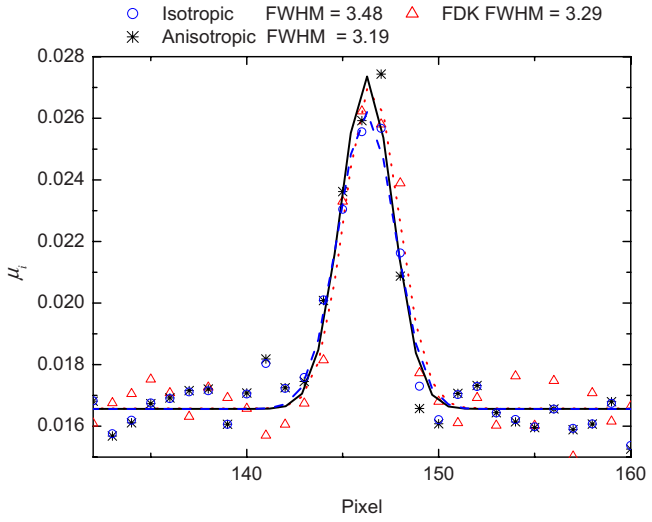

(a)

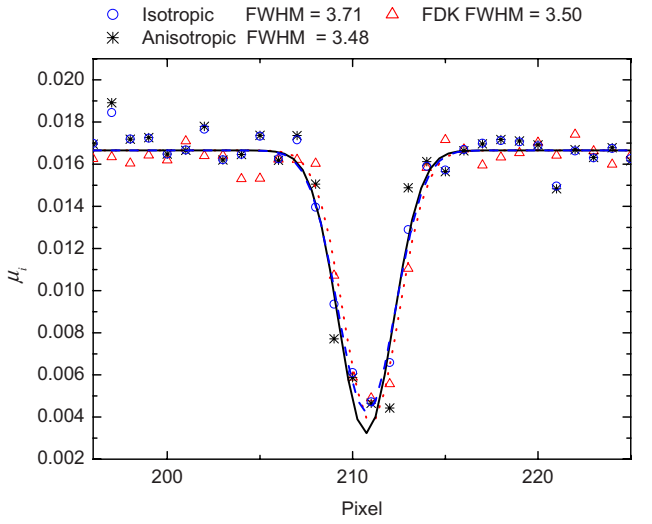

(b)

FIG. 4. Vertical profile through column 139 in Figs. 3(c) and 3(d). (a) shows the profile through the hot spot and (b) shows the profile through the cold spot. Edges are better preserved by using the anisotropic penalty as measured by the FWHM.

from 0.84 in the image reconstructed using the isotropic penalty with $\beta=1.0\times10^4$ to 2.83 in the image reconstructed using the anisotropic penalty with $\beta=30\times10^4$.

III.A.4. Comparison study with the Huber penalty

In this section, we compared the proposed anisotropic quadratic penalty with a representative edge-preserving nonquadratic penalty: the Huber penalty.[26,27] The Huber penalty function has the following form:

TABLE I. CNRs of the low-contrast ROI in Fig. 3.

β ($\times10^4$)	1	2.5	7.5	10	20	30
PWLS isotropic	0.84	0.98	1.40	1.60	2.35	3.01
PWLS anisotropic	0.77	0.82	1.04	1.20	2.22	2.83
FDK (10 mA/10 ms)				0.95		
FDK (80 mA/12 ms)				2.66		

$$H(t)=\begin{cases} t^2/2, & |t|<\theta \\ \theta(|t|-\theta)+\theta^2/2, & |t|\geqslant\theta. \end{cases} \quad (5)$$

The Huber function penalizes the difference between neighboring pixels quadratically if the absolute difference pixel value $|t|$ is smaller than some threshold θ and it will apply a linear penalty to the larger differences of $|t|\geqslant\theta$ which usually occur at edges.

Figure 3(e) shows the PWLS reconstructed CatPhan® 600 phantom by using the Huber penalty with threshold $\theta=0.001$ and the penalty parameter $\beta=35\times10^4$. It can be observed that the edges are better preserved in the images reconstructed using the Huber penalty than the images reconstructed by using the isotropic quadratic penalty. To quantitatively compare the performance of the Huber penalty and the anisotropic quadratic penalty, we calculated the MTF of the CTP591 module of the CatPhan® 600 phantom at matched noise level. Figure 5 shows the MTF curves from the proposed anisotropic quadratic penalty with penalty parameter $\beta=30\times10^4$ and the Huber penalty with threshold $\theta=0.001$. The penalty parameter β in the PWLS reconstruction with Huber penalty was set at 35×10^4 so that the noise level in the reconstructed image is matched to the anisotropic quadratic penalty. The standard deviation of the uniform region (indicated by a white square in Fig. 1) in the image reconstructed using the Huber penalty is 0.73×10^{-3} and is 0.70×10^{-3} in the image reconstructed using the anisotropic quadratic penalty. MTF curves in Fig. 5 show that the aniso-

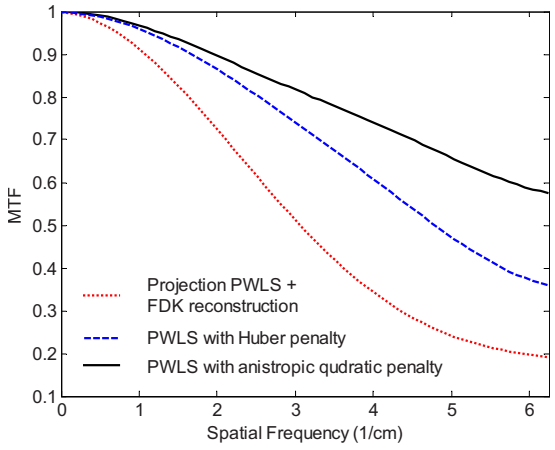

FIG. 5. MTF curves of the low-dose CBCT image reconstructed by different algorithms at a match noise level.

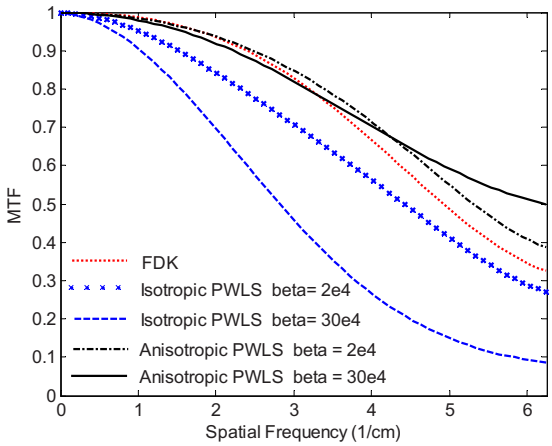

FIG. 6. MTF curves of the high-dose CBCT image reconstructed by different algorithms.

tropic quadratic penalty produces better image resolution at the matched noise level. The advantage of the anisotropic quadratic penalty may be attributed to that the Huber function depends on a hard threshold of the gradient while the anisotropic quadratic penalty considers the gradient information continuously by introducing Eq. (4).

III.A.5. Comparison with high-dose CBCT

For the projection data acquired with a tube current of 80 mA and x-ray pulse duration of 12 ms protocol, we reconstructed the CBCT image using the analytical FDK algorithm. We first compared the MTF of the image reconstructed by the analytical FDK algorithm with the image reconstructed by iterative PWLS algorithms at a matched noise level. The standard deviation of the uniform area is 5.95×10^{-4} in the FDK-reconstructed image. By setting the smoothing parameter $\beta=2\times10^4$, the standard deviation of the same region in the PWLS-reconstructed image is 5.96×10^{-4} with the isotropic penalty and 5.98×10^{-4} with the anisotropic penalty. Figure 6 shows the MTF curves from the image reconstructed by FDK and the iterative PWLS algorithms. It can be observed that the MTF of the PWLS algorithm with the anisotropic penalty is slightly better than that of the FDK algorithm, whereas the MTF of the FDK algorithm is better than that of the PWLS algorithm with isotropic penalty. This demonstrates that better spatial resolution is achieved by the PWLS algorithm using the proposed edge-preserving anisotropic penalty. The same trend can also be seen from the profiles through the pointlike objects in the CTP404 module (Fig. 4). The FWHM obtained from the fitted Gaussian function also shows that better spatial resolution is achieved by using the PWLS image reconstruction algorithm with the anisotropic penalty.

From Table I, it is seen that the CNR of the PWLS reconstructed low-dose image using the anisotropic penalty with the penalty parameter $\beta=30\times10^4$ is 2.83, which is slightly higher than that of the FDK reconstructed high-dose image—2.66. In Fig. 6, we also show the MTF curve of the PWLS algorithm using the anisotropic penalty with the penalty parameter $\beta=30\times10^4$. It can be observed that the MTF of the PWLS algorithm with the anisotropic penalty is comparable to that of the FDK algorithm. This result suggests that the PWLS iterative image reconstruction with the anisotropic penalty is capable of producing images with a CNR comparable to FDK-reconstructed high-dose images using only about 1/10 dose without sacrificing image spatial resolution.

III.B. Anthropomorphic head phantom

Results of the anthropomorphic head phantom are shown in Fig. 7. Figure 7(a) shows one slice of the image reconstructed by the analytical FDK algorithm from projection data acquired using a low-dose protocol (10 mA/10 ms); Fig. 7(b) is the FDK reconstructed image for the same phantom acquired with a high-dose protocol (80 mA/12 ms). Figure 7(c) shows the same slice of a low-dose CBCT image reconstructed by the PWLS iterative algorithm using the isotropic penalty with the penalty parameter of $\beta=30\times10^4$ and Fig. 7(d) shows the low-dose CBCT image reconstructed by the PWLS image reconstruction algorithm using the anisotropic penalty with the same penalty parameter. Figure 7(e) shows the PWLS reconstructed low-dose CBCT image using the edge-preserving Huber penalty with threshold $\theta=0.001$ and the penalty parameter $\beta=35\times10^4$. It can be observed that noise in low-dose CT images is efficiently suppressed in images reconstructed by the PWLS iterative reconstruction algorithms. The quality of low-dose CBCT reconstructed by the PWLS with anisotropic penalty is comparable to that of the high-dose FDK reconstructed image. With the anisotropic penalty in the PWLS iterative reconstruction, edges are better preserved in the reconstructed image. In the regions indicated by arrows in Fig. 7(d), it is seen that the structure is well preserved in the image reconstructed using the anisotropically penalized PWLS algorithm. The structure is blurred if the isotropic penalty was used during the PWLS reconstruction. This observation is consistent with the quantitative evaluation using the CatPhan® 600 phantom.

IV. DISCUSSION

The weighted least-squares criterion reflects that the measured data with a lower SNR will contribute less to the estimation of the attenuation map. The PWLS objective function is equivalent to the penalized maximum likelihood or maximum *a posteriori* criterion for Gaussian distributed noise. This is consistent with the observations from repeated measurements of x-ray CT projection data after logarithm transform.[7,8] The PWLS criterion for the CT projection data can also be derived from Poisson noise model of detector counts using the second-order Taylor expansion.[16] Measurement of x-ray counts can be modeled more accurately using the compound Poisson noise of polyenergetic x-ray beam

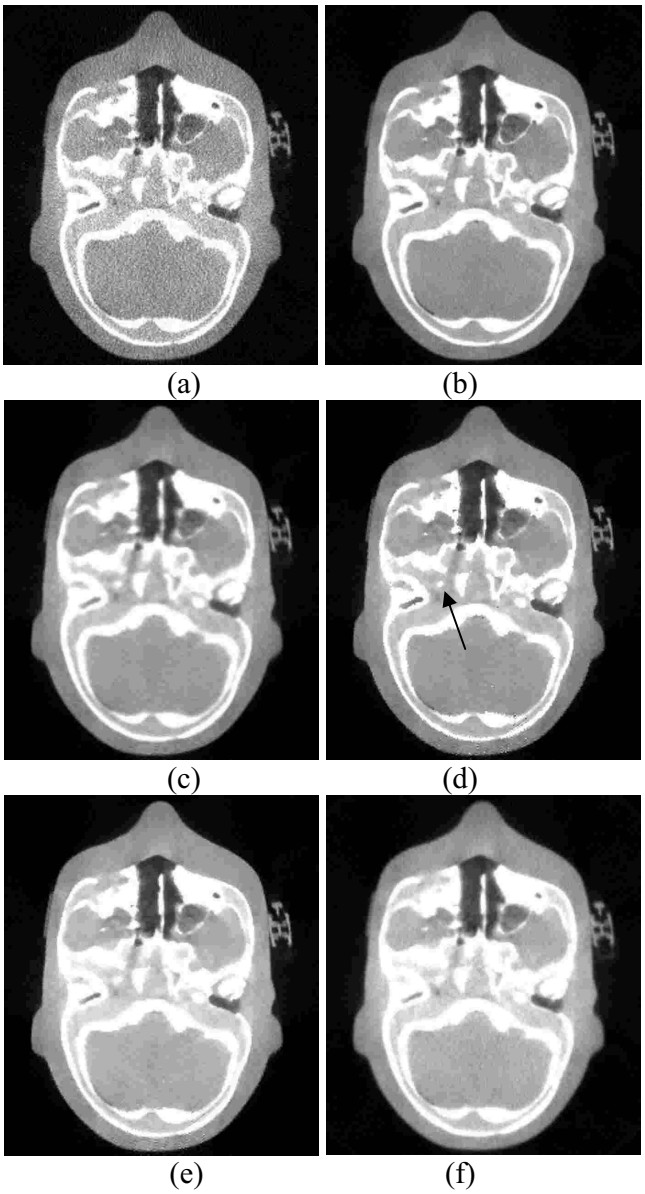

FIG. 7. CBCT of the anthropomorphic head phantom: (a) analytical FDK reconstructed image from projection data acquired using a low-dose protocol (10 mA/10 ms) and (b) a high-dose protocol (80 mA/12 ms); (c) PWLS iterative image reconstruction with an isotropic quadratic penalty from projection data acquired using a low-dose protocol and (d) with a proposed anisotropic penalty. (e) PWLS iterative image reconstruction with the Huber penalty; (f) analytical FDK reconstructed image after low-dose projection data processed by the PWLS criterion (Ref. 34) with smoothing parameter 0.09. Display window: $[0,0.02]$ mm^{-1}.

plus Gaussian electronic noise.[22] The performance of iterative reconstruction algorithms for x-ray CT may be further improved by more accurate noise modeling.

The penalty reflects the prior information of the CT images. In this work, the anisotropic penalty of the quadratic form was proposed to encourage smoothness among neighboring pixels of similar intensities but discourage the smoothness if a large difference exists between neighboring pixels. Thus, edges are better preserved in reconstructed images. In radiotherapy, CT images of the same patient are usually available before treatment. The high-quality planning CT images provide strong *a priori* information of the patient and it may be used to improve the performance of iterative image reconstruction algorithms. However, interfractional variation in treatment position and deformation of organs may make such application challenging. Dedicated registration algorithms[33] are necessary to extract information from the planning CT as a prior constraint for iterative reconstruction.

Based on the same noise properties of projection data, the PWLS objective function can also be constructed in the projection or sinogram domain where the penalty is applied between neighboring projection pixels.[34] CT images can then be reconstructed by analytical algorithms such as FDK. Compared with fully iterative image reconstruction methods, the strategy of projection smoothing followed by analytical image reconstruction is advantageous in computational efficiency because projection and backprojection cycles in the iterative image reconstruction algorithm are avoided. Recently, La Riviere and Vargas[35] have shown potential equivalence between the image-domain based iterative reconstruction methods and the strategy of sinogram restoration plus analytical filtered backprojection reconstruction. The studies performed in their work[35] are based on a simple isotropic quadratic penalty. It will be interesting to perform a similar study based on the proposed anisotropic quadratic penalty. The edge-preserving penalty in image domain may have some advantages compared with the same penalty used in projection domain because edges are better defined in the image domain than of that in the projection domain. In this work, we also included the results obtained using the strategy presented in Ref. 34, i.e., the projection image is processed according to the PWLS criterion before the analytical FDK reconstruction. Figures 3(f) and 7(f) show the results from the projection-domain approach[34] with smoothing parameter $\beta=0.09$ for the CatPhan® 600 phantom and the anthropomorphic head phantom, respectively. It can be observed that the edges in the image reconstructed by FDK from the PWLS processed projection image are blurred compared with the image reconstructed by the PWLS using the anisotropic quadratic penalty. For a quantitative comparison, we calculated the MTF and noise level of the image of CTP591 module. The MTF curve was plotted in Fig. 5 and the standard deviation around the uniform region was 0.74×10^{-3}. The MTF curves in Fig. 5 show that PWLS image reconstruction using the anisotropic quadratic penalty produces better image resolution at the matched noise level. This initial comparison study indicates that the edge-preserving penalty in the image domain produces higher image resolution than the same penalty applied in the projection domain because better edge definition is in the image domain than the projection domain.

In this work, our effort was focused on the noise suppression of CBCT using the iterative reconstruction algorithm. The presented iterative reconstruction algorithm can also be used to improve image quality of the 4D-CBCT.[36,37] In 4D-CBCT, projection views for a specific phase are usually irregular and undersampled. Direct reconstruction using the

conventional FDK algorithm from phase-binned projection data may lead to unacceptable results due to view aliasing artifacts. Several strategies, such as using slow-rotating imager[37] and interphase motion model,[38,39] have been proposed to enhance the image quality of 4D-CBCT. Iterative reconstruction algorithms incorporate both data acquisition geometry and sampling of projection views into the projection matrix automatically. Consequently, the quality of the CBCT image so obtained is generally superior over that reconstructed using an analytical method.[40]

Although iterative reconstruction algorithms have shown advantages for CT imaging in terms of noise suppression and structure preservation, computational time could be a challenge for its practical use. In our implementation, we computed the projection matrix A before iterative reconstruction. The projection matrix was stored as a file and served as a lookup table during iterations. It takes about 15 min to finish one iteration to reconstruct the CBCT images of a size $350\times350\times16$ using a PC with 3 GHz CPU. Nevertheless, the reconstruction can be sped up by graphics card acceleration[19,41] and parallel computation using PC clusters[42] and cell broadband engine.[18]

V. CONCLUSION

In this work, we presented a statistics-based iterative reconstruction algorithm for CBCT. The objective function was based on the PWLS criterion. To preserve edges in the reconstructed images, an anisotropic quadratic penalty was proposed. Noise and artifacts in low-dose CBCT are greatly suppressed using the presented PWLS reconstruction algorithm. Comparison studies with reconstruction based on the isotropic penalty have clearly shown the benefit of the proposed approach. The statistical iterative reconstruction algorithm significantly improves low-dose CBCT image quality and may find useful clinical applications in the future.

ACKNOWLEDGMENTS

This work was supported in part by grants from the Department of Defense (W81XWH-08-1-0127 and W81XWH-05-1-0041) and National Cancer Institute (1R01 CA98523 and CA104205). The authors thank Professor J. Liang from the State University of New York at Stony Brook for numerous discussions on the subject.

APPENDIX: IMAGE RECONSTRUCTION ALGORITHM

The task for image reconstruction is to estimate the attenuation coefficient distribution map μ from the projection data $\hat{p}$ by minimizing Eq. (2). In this study, the minimization was performed iteratively using the Gauss–Seidel update algorithm, similar to that in Ref. 25,

Initialization:

$$\hat{\mu}=\mathrm{FDK}\{\hat{p}\}$$
$$\hat{r}=\hat{y}-A\hat{\mu}$$
$$\Sigma=\mathrm{diag}\{\sigma_i^2(p_i)\}=\mathrm{diag}\{\exp(p_i)/N_{io}\}$$
$$s_j=a_j'\Sigma^{-1}a_j,\ \forall j,$$
$$w_{jm}'=w_{jm}\exp\left[-\left(\frac{\mu_j-\mu_m}{\delta}\right)^2\right],\ m\in N_j$$

For each iteration: (A1)

begin

For each pixel j:

begin

$$\hat{\mu}_j^{\mathrm{old}}:=\hat{\mu}_j$$
$$\alpha_j:=s_j+\beta\Sigma_{m\in N_j}w_{jm}'$$
$$\hat{\mu}_j^{\mathrm{new}}:=\frac{a_j'\Sigma^{-1}\hat{r}+s_j\hat{\mu}_j^{\mathrm{old}}+\beta\Sigma_{m\in N_j}w_{jm}'\hat{\mu}_m}{\alpha_j}$$
$$\hat{\mu}_j:=\max\{0,\hat{\mu}_j^{\mathrm{new}}\}$$
$$\hat{r}:=\hat{r}+a_j(\hat{\mu}_j^{\mathrm{old}}-\hat{\mu}_j)$$
$$w_{jm}'=w_{jm}\exp\left[-\left(\frac{\mu_j-\mu_m}{\delta}\right)^2\right],\ m\in N_j$$

end

end

The iterations can be stopped by setting a threshold for the change of objective function or the number of iterations. In all of cases presented in this work, we stopped the computation at 20 iterations at which good convergence was seen through the observation of the reconstructed image at each iteration.

[a]Author to whom correspondence should be addressed. Present address: Department of Radiation Oncology, Stanford University School of Medicine, Clinical Cancer Center, 875 Blake Wilbur Drive, Rm CC-G204, Stanford, CA 94305-5847. Telephone: (650) 498-7896; Fax: (650) 498-4015. Electronic mail: lei@reyes.stanford.edu

[1]D. A. Jaffray, J. H. Siewerdsen, J. W. Wong, and A. A. Martinez, "Flat-panel cone-beam computed tomography for image-guided radiation therapy," Int. J. Radiat. Oncol., Biol., Phys. **53**, 1337–1349 (2002).
[2]L. Lee, Q. T. Le, and L. Xing, "Retrospective IMRT dose reconstruction based on cone-beam CT and MLC log-file," Int. J. Radiat. Oncol., Biol., Phys. **70**, 634–644 (2008).
[3]M. K. Islam, T. G. Purdie, B. D. Norrlinger, H. Alasti, D. J. Moseley, M. B. Sharpe, J. H. Siewerdsen, and D. A. Jaffray, "Patient dose from kilovoltage cone beam computed tomography imaging in radiation therapy," Med. Phys. **33**, 1573–1582 (2006).
[4]N. Wen, H. Q. Guan, R. Hammoud, D. Pradhan, T. Nurushev, S. D. Li, and B. Movsas, "Dose delivered from Varian's CBCT to patients receiving IMRT for prostate cancer," Phys. Med. Biol. **52**, 2267–2276 (2007).
[5]J. Hsieh, "Adaptive streak artifact reduction in computed tomography resulting from excessive x-ray photon noise," Med. Phys. **25**, 2139–2147 (1998).
[6]M. Kachelriess, O. Watzke, and W. A. Kalender, "Generalized multi-dimensional adaptive filtering for conventional and spiral single-slice, multi-slice, and cone-beam CT," Med. Phys. **28**, 475–490 (2001).
[7]T. F. Li, X. Li, J. Wang, J. H. Wen, H. B. Lu, J. Hsieh, and Z. R. Liang, "Nonlinear sinogram smoothing for low-dose x-ray CT," IEEE Trans. Nucl. Sci. **51**, 2505–2513 (2004).
[8]J. Wang, H. B. Lu, Z. R. Liang, D. Eremina, G. X. Zhang, S. Wang, J. Chen, and J. Manzione, "An experimental study on the noise properties of x-ray CT sinogram data in Radon space," Phys. Med. Biol. **53**, 3327–3341 (2008).
[9]A. R. Depierro, "A modified expectation maximization algorithm for penalized likelihood estimation in emission tomography," IEEE Trans. Med. Imaging **14**, 132–137 (1995).
[10]R. M. Leahy and J. Y. Qi, "Statistical approaches in quantitative positron emission tomography," Stat. Comput. **10**, 147–165 (2000).
[11]J. A. Fessler and A. O. Hero, "Penalized maximum-likelihood image-reconstruction using space-alternating generalized em algorithms," IEEE

Trans. Image Process. **4**, 1417–1429 (1995).
[12]T. Li, B. Thorndyke, E. Schreibmann, Y. Yang, and L. Xing, "Model-based image reconstruction for four-dimensional PET," Med. Phys. **33**, 1288–1298 (2006).
[13]F. J. Beekman and C. Kamphuis, "Ordered subset reconstruction for x-ray CT," Phys. Med. Biol. **46**, 1835–1844 (2001).
[14]H. Erdogan and J. A. Fessler, "Ordered subsets algorithms for transmission tomography," Phys. Med. Biol. **44**, 2835–2851 (1999).
[15]J. Nuyts, B. De Man, P. Dupont, M. Defrise, P. Suetens, and L. Mortelmans, "Iterative reconstruction for helical CT: A simulation study," Phys. Med. Biol. **43**, 729–737 (1998).
[16]K. Sauer and C. Bouman, "A local update strategy for iterative reconstruction from projections," IEEE Trans. Signal Process. **41**, 534–548 (1993).
[17]J. Wang, T. Li, H. B. Lu, and Z. R. Liang, "Penalized weighted least-squares approach to sinogram noise reduction and image reconstruction for low-dose x-ray computed tomography," IEEE Trans. Med. Imaging **25**, 1272–1283 (2006).
[18]M. Knaup, W. A. Kalender, and M. Kachelrieb, "Statistical cone-beam CT image reconstruction using the cell broadband engine," IEEE Nuclear Science Symposium Conference Record **5**, 2837–2840 (2006).
[19]F. Xu and K. Mueller, "Accelerating popular tomographic reconstruction algorithms on commodity PC graphics hardware," IEEE Trans. Nucl. Sci. **52**, 654–663 (2005).
[20]J. B. Thibault, K. D. Sauer, C. A. Bouman, and J. Hsieh, "A three-dimensional statistical approach to improved image quality for multislice helical CT," Med. Phys. **34**, 4526–4544 (2007).
[21]J. Song, Q. H. Liu, G. A. Johnson, and C. T. Badea, "Sparseness prior based iterative image reconstruction for retrospectively gated cardiac micro-CT," Med. Phys. **34**, 4476–4483 (2007).
[22]B. R. Whiting, P. Massoumzadeh, O. A. Earl, J. A. O'Sullivan, D. L. Snyder, and J. F. Williamson, "Properties of preprocessed sinogram data in x-ray computed tomography," Med. Phys. **33**, 3290–3303 (2006).
[23]P. Sukovic and N. H. Clinthorne, "Penalized weighted least-squares image reconstruction for dual energy x-ray transmission tomography," IEEE Trans. Med. Imaging **19**, 1075–1081 (2000).
[24]P. J. La Riviere, J. G. Bian, and P. A. Vargas, "Penalized-likelihood sinogram restoration for computed tomography," IEEE Trans. Med. Imaging **25**, 1022–1036 (2006).
[25]J. A. Fessler, "Penalized weighted least-squares image-reconstruction for positron emission tomography," IEEE Trans. Med. Imaging **13**, 290–300 (1994).
[26]I. A. Elbakri and J. A. Fessler, "Statistical image reconstruction for polyenergetic x-ray computed tomography," IEEE Trans. Med. Imaging **21**, 89–99 (2002).
[27]W. Chlewicki, F. Hermansen, and S. B. Hansen, "Noise reduction and convergence of Bayesian algorithms with blobs based on the Huber function and median root prior," Phys. Med. Biol. **49**, 4717–4730 (2004).
[28]S. Geman and D. Geman, "Stochastic relaxation, Gibbs distributions, and the Bayesian restoration of images," IEEE Trans. Pattern Anal. Mach. Intell. **6**, 721–741 (1984).
[29]D. Geman and G. Reynolds, "Constrained restoration and the recovery of discontinuities," IEEE Trans. Pattern Anal. Mach. Intell. **14**, 367–383 (1992).
[30]P. Charbonnier, L. BlancFeraud, G. Aubert, and M. Barlaud, "Deterministic edge-preserving regularization in computed imaging," IEEE Trans. Image Process. **6**, 298–311 (1997).
[31]G. Han, Z. Liang, and J. You, "A fast ray-tracing technique for TCT and ECT studies," IEEE Nuclear Science Symposium Conference Record **3**, 1515–1518 (1999).
[32]P. Perona and J. Malik, "Scale-space and edge-detection using anisotropic diffusion," IEEE Trans. Pattern Anal **12**, 629–639 (1990).
[33]E. Schreibmann, B. Thorndyke, T. Li, J. Wang, and L. Xing, "Four-dimensional image registration for IGRT," Int. J. Radiat. Oncol., Biol., Phys. **71**, 578–586 (2008).
[34]J. Wang, T. Li, Z. Liang, and L. Xing, "Dose reduction for kilovoltage cone-beam computed tomography in radiation therapy," Phys. Med. Biol. **53**, 2897–2909 (2008).
[35]P. J. La Riviere and P. Vargas, "Potential equivalence of sinogram and image-domain penalized likelihood methods," IEEE Nuclear Science Symposium Conference Record, 2007, NSS '07, 6, 4169–4173 (2007).
[36]T. Li, L. Xing, P. Munro, C. McGuinness, M. Chao, Y. Yang, B. Loo, and A. Koong, "Four-dimensional cone-beam computed tomography using an on-board imager," Med. Phys. **33**, 3825–3833 (2006).
[37]T. Li and L. Xing, "Optimizing 4D cone-beam CT acquisition protocol for external beam radiotherapy," Int. J. Radiat. Oncol., Biol., Phys. **67**, 1211–1219 (2007).
[38]R. Zeng, J. A. Fessler, and J. M. Balter, "Estimating 3-D respiratory motion from orbiting views by tomographic image registration," IEEE Trans. Med. Imaging **26**, 153–163 (2007).
[39]T. Li, A. Koong, and L. Xing, "Enhanced 4D cone-beam CT with inter-phase motion model," Med. Phys. **34**, 3688–3695 (2007).
[40]G.-H. Chen, J. Tang, and S. Leng, "Prior image constrained compressed sensing (PICCS): A method to accurately reconstruct dynamic CT images from highly undersampled projection data sets," Med. Phys. **35**, 660–663 (2008).
[41]Z. Wang, G. Han, T. Li, and Z. Liang, "Speedup OS-EM image reconstruction by PC graphics card technologies for quantitative SPECT with varying focal-length fan-beam collimation," IEEE Trans. Nucl. Sci. **52**, 1274–1280 (2005).
[42]X. Li, J. Ni, and G. Wang, "Parallel iterative cone-beam CT image reconstruction on a PC cluster," J. X-Ray Sci. Technol. **13**, 63–72 (2005).

Noise suppression in scatter correction for cone-beam CT

Lei Zhu,[a] Jing Wang, and Lei Xing
Department of Radiation Oncology, Stanford University, Stanford, California 94305

(Received 23 July 2008; revised 10 December 2008; accepted for publication 11 December 2008; published 10 February 2009)

Scatter correction is crucial to the quality of reconstructed images in x-ray cone-beam computed tomography (CBCT). Most of existing scatter correction methods assume smooth scatter distributions. The high-frequency scatter noise remains in the projection images even after a perfect scatter correction. In this paper, using a clinical CBCT system and a measurement-based scatter correction, the authors show that a scatter correction alone does not provide satisfactory image quality and the loss of the contrast-to-noise ratio (CNR) of the scatter corrected image may overwrite the benefit of scatter removal. To circumvent the problem and truly gain from scatter correction, an effective scatter noise suppression method must be in place. They analyze the noise properties in the projections after scatter correction and propose to use a penalized weighted least-squares (PWLS) algorithm to reduce the noise in the reconstructed images. Experimental results on an evaluation phantom (Catphan©600) show that the proposed algorithm further reduces the reconstruction error in a scatter corrected image from 10.6% to 1.7% and increases the CNR by a factor of 3.6. Significant image quality improvement is also shown in the results on an anthropomorphic phantom, in which the global noise level is reduced and the local streaking artifacts around bones are suppressed. [DOI: 10.1118/1.3063001]

I. INTRODUCTION

In x-ray computed tomography (CT), scatter causes severe distortions and contrast loss in the reconstructed images.[1,2] Scatter magnitude increases as the x-ray illuminated volume size increases.[3] In an x-ray system with a large area detector, such as a cone-beam CT (CBCT) system, the scatter-to-primary ratio (SPR) can be as high as 8 in certain areas of the projection images.[4,5]

CBCT is being commonly used in many applications for its large volume coverage. However, the high SPR severely deteriorates the quality of CBCT image and hampers its clinical usage. Many scatter correction methods have been proposed in the literature, and research in this field is still very active.[4,6–9] There are two major types of scatter removal techniques. The first type performs scatter suppression during the acquisition of projection data, based on the difference between the incident angles of primary photons and scatter photons. Typical examples include the antiscatter grid method and the air gap method.[10,11] Although instant scatter suppression is achieved using these methods, their efficacy is usually limited. Siewerdsen *et al.*, for example, showed that an antiscatter grid was effective only in improving the contrast-to-noise ratio (CNR) of low resolution CT images.[11] Kyriakou *et al.* also reported that if an antiscatter grid is used and the scatter is high, the imaging dose need to be increased significantly to compensate for the primary loss due to the insertion of the grid.[12] An improved scatter correction capability has been demonstrated using the scatter correction methods in the second category, where the scatter is corrected using postprocessing techniques on the scatter contaminated projection images.[9,13–15] Due to the randomness of scattering events, however, these methods implicitly or explicitly assume smooth scatter distributions and tacitly ignore the existence of high-frequency scatter noise. The scatter noise is therefore left in the image after scatter correction, resulting a degradation of CNRs in the reconstructed images.[16] So far, the noise due to scatter in the x-ray projection image is generally considered as a low-dose imaging problem, and little attention has been paid in the literature to reduce the noise due to scatter correction. As the scatter correction techniques become more successful, this issue is becoming increasingly important.

The purpose of this paper is to investigate the role of high-frequency noise in the CB projection image after scatter correction and to provide a practical solution to noise suppression in scatter corrected reconstructed images. We first study the noise property of the projection images after scatter correction according to Poisson statistics. A penalized weighted least-squares (PWLS) algorithm is then applied to effectively suppress the image noise.[17] The algorithm is evaluated using phantom experiments on a clinical CBCT system.

II. METHOD

II.A. Noise in x-ray projections with and without scatter correction

There are two major types of noise in x-ray projection images. One is the image independent noise due to the electrical and roundoff error, which can be considered as Gaussian noise; the other is the image dependent noise due to the statistical fluctuation of the x-ray photons that exit an object, which can be considered as Poisson noise.[18] We assume the noise of the first type is small and consider only the Poisson noise here.

Denote variables s and p as the detected scatter and primary signals with mean values S and P, respectively. s and p are Poisson distributed, i.e., $s \sim \text{Poisson}(S)$ and p

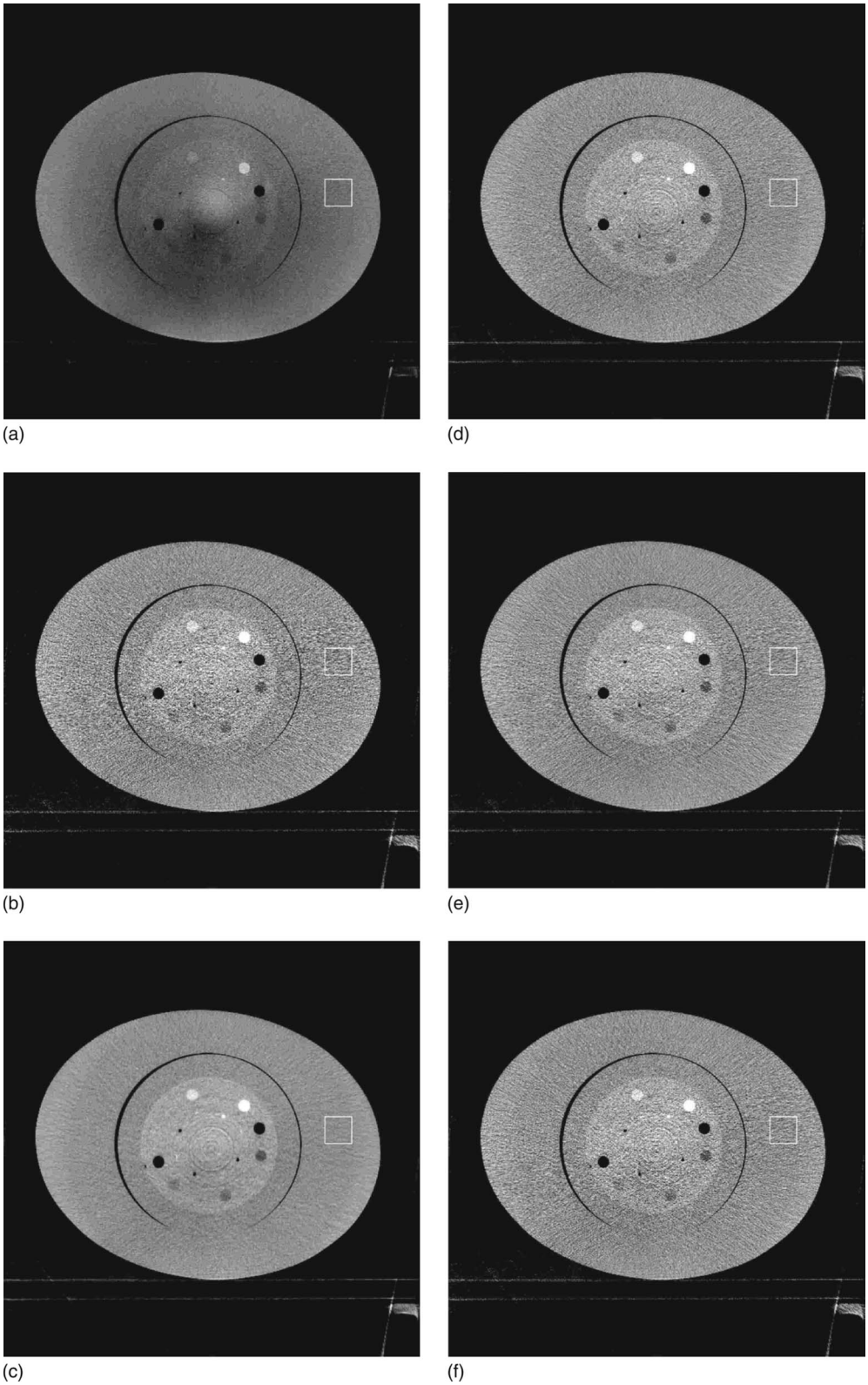

FIG. 1. Reconstructed images of the Catphan©600 phantom with an oval body annulus. Display window: [−500 500] HU. The mean and standard deviation (std) inside the white squares in the images are measured as *mean*+*std* HU. (a) No scatter correction and no noise suppression; CT number in the selected ROI (white square): -117 ± 51 HU. (b) Scatter correction without noise suppression; CT number in the ROI: 17 ± 191 HU. (c) Scatter correction using the proposed noise suppression algorithm, $\beta = 0.0009$; CT number in the ROI: 18 ± 52 HU. (d) Scatter correction using the proposed noise suppression algorithm, $\beta = 0.0001$; CT number in the ROI: 16 ± 108 HU. (e) Scatter correction with noise suppression using the standard Hamming filter; CT number in the ROI: 18 ± 152 HU. (f) Scatter correction using the proposed noise suppression algorithm, assuming $s_e = 0$; CT number in the ROI: 18 ± 151 HU.

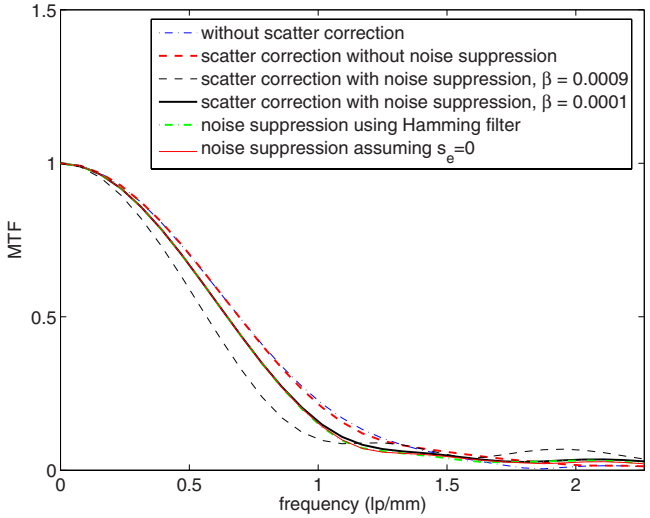

FIG. 2. Measured MTFs using the Catphan©600 phantom. The algorithm parameters are tuned such that the last three curves as shown in the legend match.

$\sim$Poisson(P). From the fact that the point spread function of the scatter is broad and smooth,[19] we assume s is independent of p, and therefore, $(s+p)\sim$Poisson$(S+P)$. Denote n_s and n_p as the statistical noises of the scatter and primary, respectively, and one obtains

$$s = S + n_s,$$
$$p = P + n_p. \tag{1}$$

Due to Poisson statistics,

$$\mathrm{var}(n_s) = S,$$
$$\mathrm{var}(n_p) = P. \tag{2}$$

Denoting I_0 as the incident photon intensity and q as the line integral image without scatter correction, we have

$$\begin{aligned} q &\equiv \ln\left(\frac{I_0}{s+p}\right) \\ &= -\ln(s+p) + \ln(I_0) \\ &= -\ln(S+P) + \ln(I_0) - \frac{1}{S+P}(n_s+n_p) + O((n_s+n_p)^2). \end{aligned} \tag{3}$$

The last step uses Taylor's expansion at $(S+P)$.

Since I_0 is typically very large, the noise associated with $\log(I_0)$ can be ignored. Assume (n_s+n_p) is small and ignore the high order term, then the noise of q, n_{nc}, and its variance are approximated as

$$n_{\mathrm{nc}} \approx -\frac{1}{S+P}(n_s+n_p), \tag{4}$$

$$\begin{aligned} \mathrm{var}(n_{\mathrm{nc}}) &\approx \frac{1}{(S+P)^2}\mathrm{var}(n_s+n_p) \\ &= \frac{1}{(S+P)^2}(S+P) \\ &= \frac{1}{S+P}. \end{aligned} \tag{5}$$

When an effective scatter correction algorithm is applied, the scatter mean value S is removed, while the high-frequency noise n_s is left in the corrected image. Similarly, the scatter corrected line integral image q_c can be written as

$$\begin{aligned} q_c &\equiv \ln\left(\frac{I_0}{s+p-S}\right) \\ &= \ln\left(\frac{I_0}{n_s+n_p+P}\right) \\ &= -\ln(n_s+n_p+P) + \ln(I_0) \\ &= -\ln(P) + \ln(I_0) - \frac{1}{P}(n_s+n_p) + O((n_s+n_p)^2). \end{aligned} \tag{6}$$

The associated noise n_c and its variance is approximated as

$$n_c \approx -\frac{1}{P}(n_s+n_p)$$

$$\begin{aligned} \mathrm{var}(n_c) &\approx \frac{1}{P^2}\mathrm{var}(n_s+n_p) \\ &= \frac{1}{P^2}(S+P) \\ &= \frac{1}{S+P}\left(1+\frac{S}{P}\right)^2. \end{aligned} \tag{7}$$

Therefore, the ratio of the variances of n_c and n_{nc} is

$$\frac{\mathrm{var}(n_c)}{\mathrm{var}(n_{\mathrm{nc}})} \approx \left(1+\frac{S}{P}\right)^2. \tag{8}$$

Equation (8) shows that the noise is magnified after a scatter correction is applied on the projection image. Since the noise-free scatter signal S is spatially much smoother than the noise-free primary signal P, the spatial distribution of SPR (S/P) is typically nonuniform. In a projection image on a human chest, for example, the SPR value is very low around the object boundary (less than 0.2) and can be larger than 8 in areas of small primary signals (e.g., behind bones). As a result, the noise variance magnification across the projection image ranges from below 1.5 to more than 80. As will be shown in Sec. III, the nonuniform noise magnification not only increases the noise level in the reconstructed image but also results in local streaking artifacts.

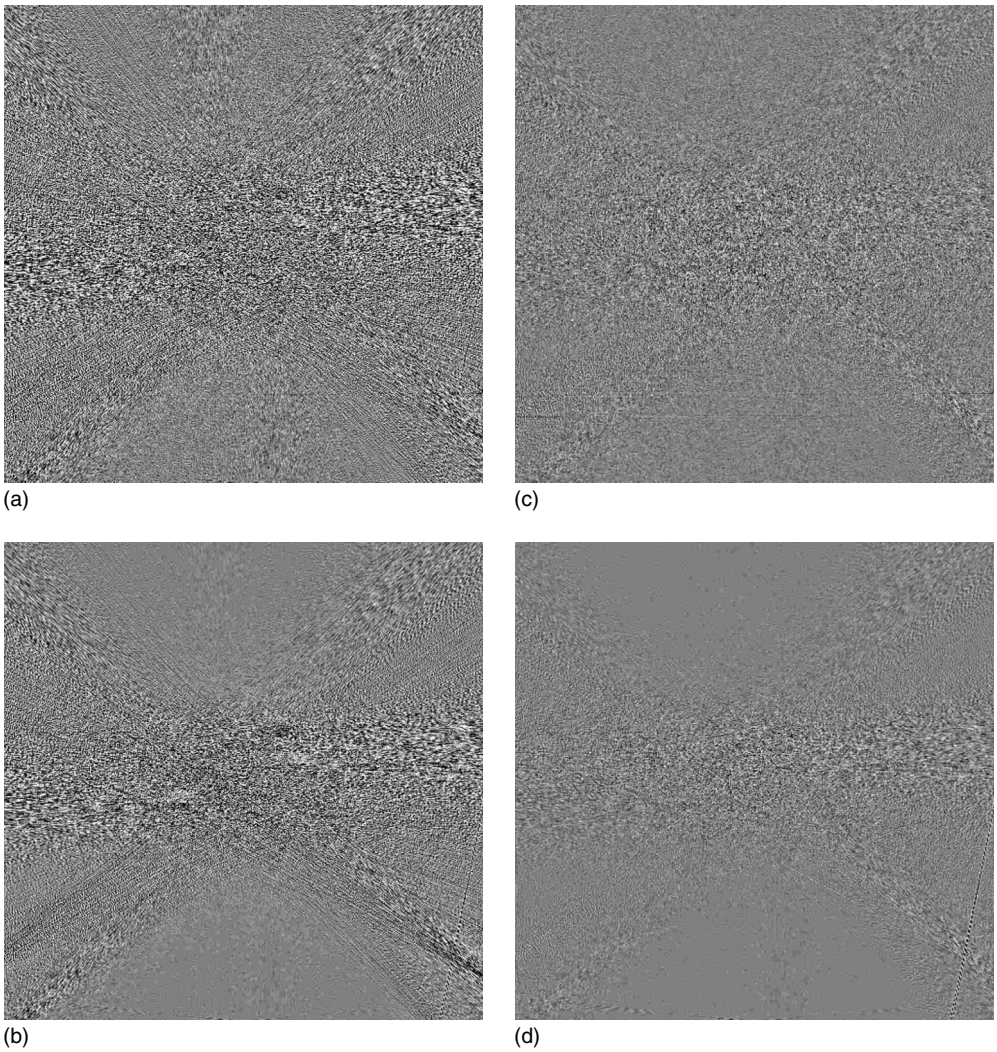

FIG. 3. Difference images after applying noise suppression on Fig. 1(b) using different algorithms. Display window: [−150 150] HU. (a) Scatter correction using the proposed noise suppression algorithm, $\beta=0.0009$. [Fig. 1(c)–Fig. 1(b)]. (b) Scatter correction using the proposed noise suppression algorithm, $\beta=0.0001$. [Fig. 1(d)–Fig. 1(b)]. (c) Scatter correction with noise suppression using the standard Hamming filter [Fig. 1(e)–Fig. 1(b)]. (d) Scatter correction using the proposed noise suppression algorithm, assuming $s_e=0$. [Fig. 1(f)–Fig. 1(b)].

II.B. The noise suppression algorithm

Based on the noise property of the scatter corrected image as derived in Eq. (7), we modify and implement a previously developed penalized weighted least-squares (PWLS) method[20] to suppress the image noise. The PWLS method is a statistics-based algorithm that aims to estimate the ideal linear integrals by minimizing the PWLS objective function. The PWLS objective function models the first and second moments of the projection data. Mathematically, the PWLS cost function is written as

$$\phi(\widehat{q_c}) = (q_c - \widehat{q_c})^T \Sigma^{-1} (q_c - \widehat{q_c}) + \beta R(\widehat{q_c}). \tag{9}$$

The first term in Eq. (9) is a weighted least-squares criterion. The variable q_c is the vector of the scatter corrected line integral data as shown in Eq. (6); the variable $\hat{q}_c$ is the vector of noise suppressed line integral data to be estimated. The symbol T denotes the transpose operator. The matrix Σ is diagonal matrix and its ith element is the variance of q_c at detector pixel i. From Eq. (7), we approximate the variance of q_c based on the following equations:

$$p_m \approx S + P$$

$$\begin{aligned} \mathrm{var}(q_c) &= \mathrm{var}(n_c) \\ &\approx \frac{1}{S+P}\left(1+\frac{S}{P}\right)^2 \\ &\approx \frac{1}{p_m}(1+SPR)^2 \end{aligned} \tag{10}$$

$$\begin{aligned} &\approx \frac{1}{p_m}\left(\frac{p_m}{p_m - s_e}\right)^2 \\ &\approx \frac{p_m}{(p_m - s_e)^2}, \end{aligned} \tag{11}$$

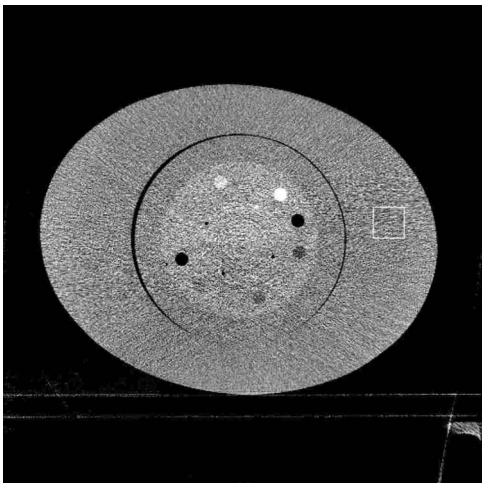

(a)

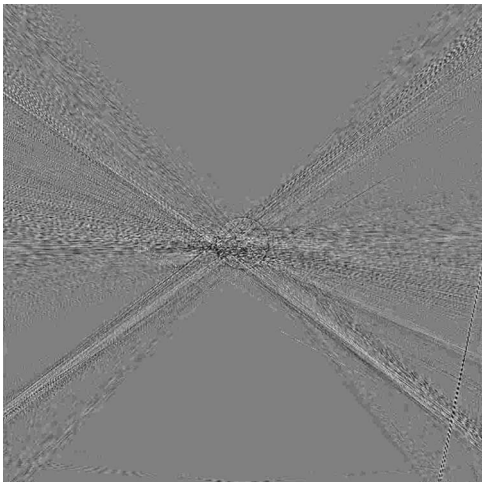

(b)

FIG. 4. Reconstruction of the Catphan©600 phantom using the proposed algorithm with an accurate scatter estimate in the scatter correction but an inaccurate scatter estimate in the noise suppression. (a) Noise suppression using the proposed algorithm, assuming scatter to be a constant fraction of the smallest intensity in each projection; CT number in the ROI: 15 ± 183 HU. Display window: [−500 500] HU. (b) Difference image [Fig. 4(a)–Fig. 1(b)]. Display window: [−150 150] HU.

where p_m is the measured projection data before scatter correction and logarithm operation; s_e is the scatter estimate obtained from scatter correction algorithms. With the nonuniform weights included in the least-squares criterion, the data with lower signal-to-noise ratios (SNR) contribute less for estimation of the noise suppressed line integrals.

The second term in Eq. (9) is a smoothness penalty or a prior constraint, where β is the smoothing parameter which controls the degree of agreement between the estimated and the measured data. A quadratic function as used in the previous publications[21] is adopted here,

$$R(q) = \sum_i \sum_n w_{in}(q_i - q_n)^2, \tag{12}$$

where n represents four nearest neighbors around pixel i and w_{in} is the weight for neighbor n. To preserve the edge information, anisotropic weights are used as w_{in}. The weight of the neighbor is determined by the magnitude of difference between neighbors and the pixel of concern,

$$w_{in} = \exp\left(-\left(\frac{q_i - q_n}{\delta}\right)^2\right), \tag{13}$$

where δ is another user-defined parameter which controls the strength of edge preservation.

In our implementations, the parameter δ was chosen as such a value that 90% of the sinogram pixels in the projection images to be processed has a gradient magnitude smaller than δ.[22] The cost function (9) is minimized efficiently using an iterative Gauss–Seidel updating strategy.[21] If standard CBCT imaging parameters are used, the algorithm converges to an optimal solution typically after about 20 iterations. On a 3.0 GHz PC, the process takes about 3 s on each projection image.

II.C. Scatter estimation

In this work, we use a measurement-based method for scatter estimation. In each experiment, a lead strip was inserted between the x-ray source and the object, resulting in a horizontal strip shadow on the detector with a width of approximately 2 cm. Since the lead strip attenuates almost all the incident photons, the signal detected inside the strip shadow only contains scatter. Assuming that the scatter distributions with and without the insertion of the lead strip are approximately the same, we consider the measured scatter signals using a lead strip as the scatter signals in a conventional scan at the same location. To get rid of the noise in the measurement, the detected signals inside the 2 cm strip shadow were first averaged in the longitudinal direction and then smoothed laterally using a moving average filter. The resultant signal was used as the scatter estimate in a following conventional scan.

II.D. Evaluation

The proposed method is evaluated using experiments on a Varian Acuity CT simulator (Varian Medical Systems, Palo Alto, CA). This CBCT imaging system is commonly used in radiation therapy for verifying the patient geometry. A standard protocol as used in clinic was used in the experiments. The x-ray tube operated at 125 kVp voltage and 80 mA with the pulse width at each projection angle of 25 ms. Data of a 360° scan consist of about 680 projections with an angle interval of about 0.5°. The dimension of each acquired projection image was 397.3×298.0 mm^2, containing 1024×768 pixels. The source-to-axis distance (SAD) was 1000 mm and the source-to-imager distance (SID) was 1500 mm. To increase the field of view (FOV), a half-fan mode was used, with the flat-panel detector shifted by approximately 160 mm.

Two phantoms were used in the experiments. The first was an evaluation phantom which consisted of a Catphan©600 phantom in the middle with a radius of 10 cm and an oval body annulus in the periphery to expand the phantom to an elliptical cylinder with a major axis of 38 cm and a

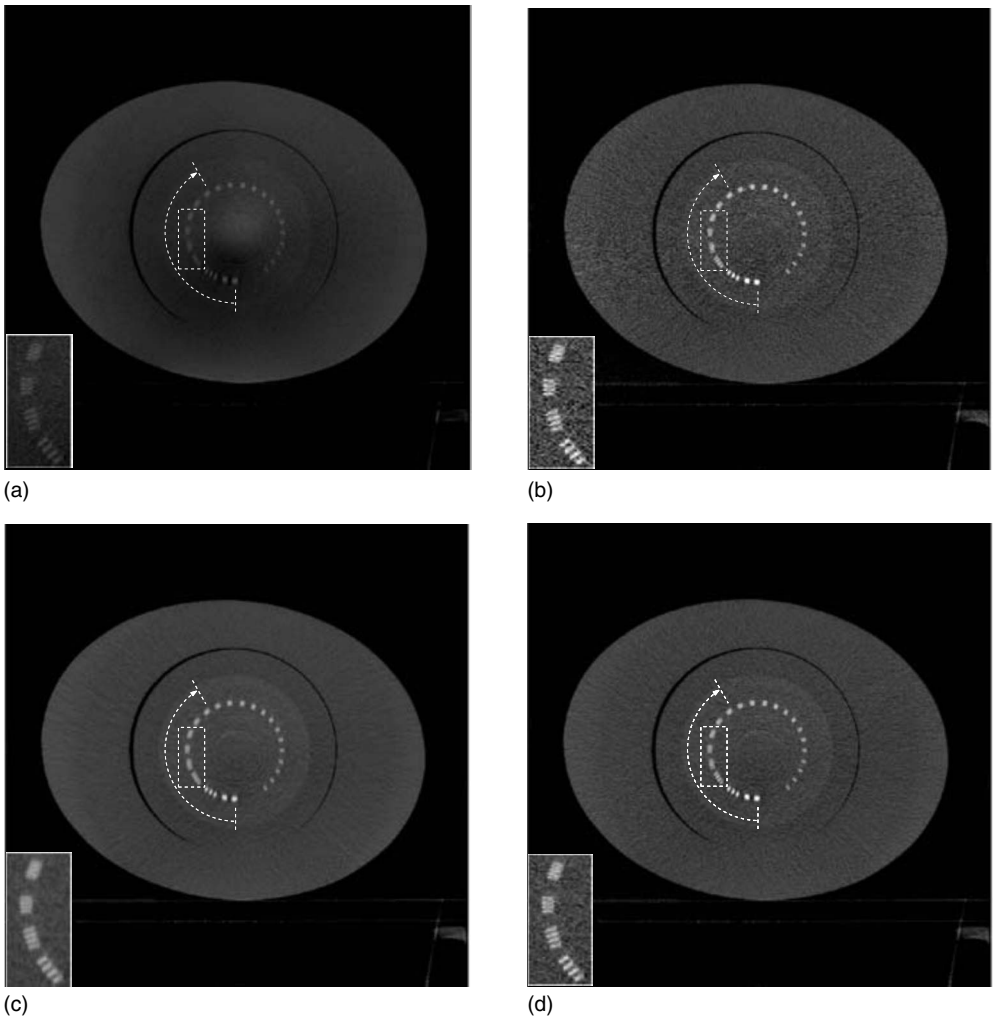

FIG. 5. Reconstructed images of the Catphan©600 phantom with an oval body annulus. Display window: [−500 1700] HU. A different slice from Fig. 1 is shown to investigate the resolution performance. A zoom-in image of the line pairs inside the dashed rectangle is shown at the lower left corner in each image. The dashed arcs indicate the sets of line pairs, of which 1D profiles passing through the center are compared in Fig. 6. (a) No scatter correction and no noise suppression. (b) Scatter correction without noise suppression. (c) Scatter correction using the proposed noise suppression algorithm, $\beta=0.0009$. (d) Scatter correction using the proposed noise suppression algorithm, $\beta=0.0001$.

minor axis of 30 cm. The uniform oval annulus is made of the same material as that of the CTP 486 uniformity test module inside the standard Catphan©600 phantom, and it has an estimated CT number of ~15 Hounsfield Units (HU). Due to the increased volume size, scatter was high in the scan and the image quality was much worse than that when only the Catphan©600 phantom was imaged. No bow-tie filter was used in the experiments. The second phantom was an anthropomorphic chest phantom. A bow-tie filter as used in clinic was placed on in order to maintain a more uniform photon statistics across the FOV. The reconstructed images are presented in HU, i.e., with a CT number of −1000 HU for air and a CT number of 0 HU for water-equivalent materials.

Images are reconstructed using the standard FDK algorithm,[23] without scatter correction and noise suppression, with scatter correction but without noise suppression, and with scatter correction and the proposed noise suppression using different β values. The same filters are used in all the reconstructions. To demonstrate the advantage of the proposed algorithm on noise suppression, two more reconstructions of the Catphan©600 phantom are carried out with the same scatter correction. For a fair comparison, the noise suppression parameters in these reconstructions are adjusted such that the corresponding modulation transfer functions (MTF) approximately match, indicating a similar spatial resolution performance. The first reconstruction uses a standard low-pass Hamming filter in the filtering step in the FDK algorithm to suppress the projection noise. The second reconstruction assumes zero scatter in the noise suppression step after the scatter correction and directly uses the previously developed PWLS algorithm for the noise suppression, i.e., assuming $s_e=0$ in Eq. (11). The tungsten carbide inside the Catphan©600 phantom with a diameter of 0.28 mm is used for the MTF measurements.

Side-by-side comparisons of reconstructed images are provided to illustrate the performance on noise reduction in the proposed algorithm as well as its effect on the image

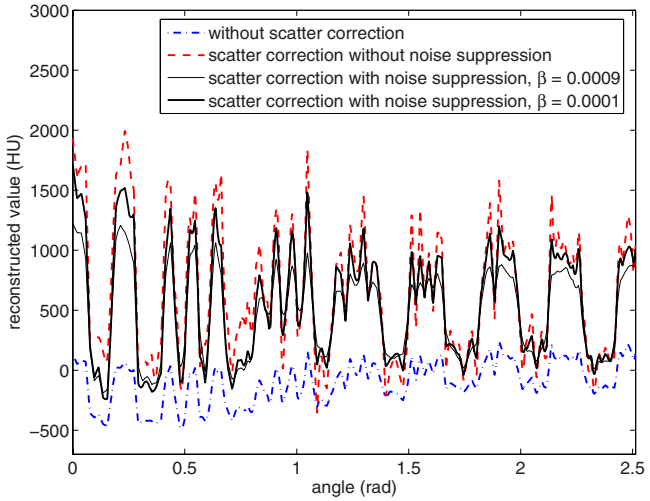

FIG. 6. Comparison of 1D profiles passing through the center of the line pairs indicated by the dashed arcs shown in Fig. 5.

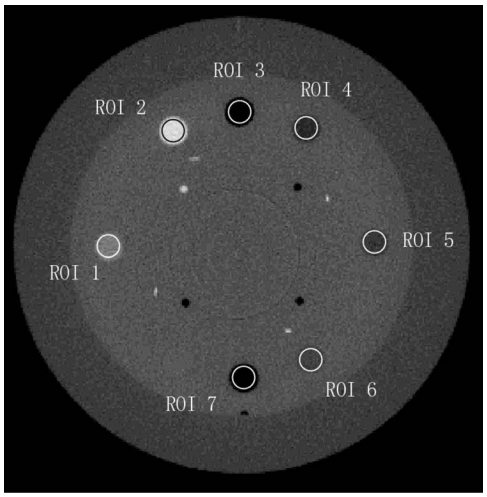

FIG. 7. Catphan image without the oval body annulus used as the benchmark. A narrow collimator was also used to further reduce the scatter artifacts. Seven ROIs are used in the quantitative analysis.

resolution. Difference images before and after noise suppression are also presented. In the quantitative analysis, besides image noise levels, image contrasts and CNRs in selected regions of interest (ROI) with relatively uniform reconstructed values are used. The image contrast is defined as

$$\text{contrast} = \mu_r - \mu_b, \tag{14}$$

where μ_r is the mean reconstructed value inside the ROI and μ_b is the mean reconstructed value in the surrounding area. The CNR is defined as

$$\text{CNR} = \frac{|\mu_r - \mu_b|}{\sqrt{\frac{\sigma_r^2 + \sigma_b^2}{2}}}, \tag{15}$$

where σ_r^2 is the variance inside the ROI and σ_b^2 is the variance in the surrounding area.

III. RESULTS

Figure 1 shows the reconstructed images of the Catphan©600 phantom with an oval annulus. The image distortion is obvious in Fig. 1(a), where no scatter correction is applied. Most of the shading artifacts due to scatter are eliminated using the measurement-based scatter correction, as shown in Fig. 1(b). However, the noise is magnified in the scatter corrected image and the image quality is degraded. Figures 1(c) and 1(d) are the images with noise suppressed using the proposed method. To investigate the performance of the algorithm on noise reduction and image resolution, two different β values are used. The first value is relatively large, and generates an image [Fig. 1(c)] with approximately the same noise level in the selected ROI as that in the image without scatter correction and noise suppression. The improvement of image quality is significant. A small β value is used in the second implementation of the noise suppression algorithm. This value achieves a less smoothed image as seen in Fig. 1(d). Figure 1(e) is the result using a standard Hamming filter on the projection images for noise suppression. Figure 1(f) is the result using the previously developed PWLS algorithm. Equivalently, we assume $s_e = 0$ in Eq. (11) of the proposed algorithm. The MTFs of the six reconstructions are measured and shown in Fig. 2. Note that we adjust the noise suppression parameters such that Figs. 1(d)–1(f) have approximately the same MTF curves. With similar performances on image resolution, Hamming filtering and the previously developed PWLS method reduce the noise standard deviation in the selected ROI from 191 HU to approximately 150 HU, and the proposed algorithm is able to further reduce the noise standard deviation down to 108 HU. An improved image quality using the proposed algorithm is also evident in the comparison shown in Fig. 1. Figure 3 shows the difference images of the same slice as in Fig. 1 before and after noise suppression using different algorithms as described above.

Figure 1(f) indicates that it is important to include the scatter estimate in the proposed noise suppression algorithm. Although scatter estimation/correction algorithms are now becoming more and more successful, it is still challenging to achieve an accurate scatter estimate in many applications. Another reconstruction is carried out to study the sensitivity of the proposed algorithm performance with respect to the accuracy of the scatter estimation. When scatter correction is inaccurate, residual scatter artifacts are dominant as compared to the image noise. For a better illustration of the algorithm performance on noise suppression, we use an accurate scatter estimate for the scatter correction. In the noise suppression step using the proposed algorithm, we assume that scatter is uniform over the whole field and it equals a constant fraction of the smallest intensity in each projection. The algorithm parameters are tuned such that the corresponding MTF curve matches those of Figs. 1(d)–1(f). The reconstructed image and its difference image as compared to the result without noise suppression [Fig. 1(b)] are shown in Fig. 4. The inaccurate scatter estimation not only significantly compromises the noise suppression capability of the

TABLE I. Contrast comparison of the selected ROIs (HU). The values in parentheses are the relative errors in percentage (absolute values) with respect to the benchmark image shown in Fig. 7.

ROI	1	2	3	4
No scatter correction [Fig. 1(a)]	83 (66.1%)	302 (65.0%)	−421 (60.7%)	−98 (64.2%)
Scatter correction only [Fig. 1(b)]	283 (15.7%)	998 (13.3%)	−1131 (5.5%)	−279 (2.2%)
Proposed algorthum, β=0.0009 [Fig. 1(c)]	261 (6.4%)	873 (1.1%)	−1069 (0.2%)	−272 (0.5%)
Proposed algorithm, β=0.0001 [Fig. 1(d)]	267 (9.3%)	876 (1.5%)	−1067 (0.5%)	−270 (1.3%)
Using a Hamming filter [Fig. 1(e)]	284 (15.9%)	958 (11.0%	−1123 (4.8%)	−282 (3.0%)
Proposed algorithm, s_e=0 [Fig. 1(f)]	281 (14.9%)	956 (10.8%)	−1123 (4.8%)	−279 (1.9%)
Benchmark (Fig. 7)	245	863	−1072	−273

ROI	5	6	7	mean error
No scatter correction [Fig. 1(a)]	−61 (67.6%)	−37 (70.0%)	−334 (67.9%)	65.9%
Scatter correction only [Fig. 1(a)]	−213 (12.6%)	−96 (22.8%)	−1058 (1.9%)	10.6%
Proposed algorithm, β=0.0009 [Fig. 1(c)]	−190 (0.7%)	−121 (2.8%)	−1037 (0.1%)	1.7%
Proposed algorithm, β=0.0001 [Fig. 1(d)]	−202 (6.7%)	−102 (18.3%)	−1010 (2.7%)	5.8%
Using a Hmming filter [Fig. 1(e)]	−209 (10.4%)	−116 (6.9%)	−1075 (3.5%)	7.9%
Proposed algorithm, s_e=0 [Fig. 1(f)]	−209 (10.8%)	−104 (16.9%)	−1065 (2.5%)	8.9%
Benchmark (Fig. 7)	−189	−125	−1038	

proposed algorithm [the noise standard deviation in the selected ROI of Fig. 4(a) is 183 HU] but also results in additional streaking artifacts which are evident in the difference image [Fig. 4(b)]. It is interesting to note that the proposed algorithm with a zero scatter estimate [Fig. 1(f)] performs better than that with a uniform scatter estimate [Fig. 4(a)]. The main reason is that the performance of the proposed algorithm is determined by the estimation accuracy of the spatial distribution of the image noise, instead of the total magnitude. Using a constant fraction of the smallest intensity in each projection as the scatter estimate gives a better estimate on the total image noise magnitude than using zero scatter estimates. However, it results in a spatial distribution of noise variance more different from the truth. More discussion on this issue will follow in a later section.

To further investigate the image resolution with respect to the β values, Fig. 5 shows the reconstructed slices with the resolution gauges. Note that a display window different from that in Fig. 1 is used for a better display of the line pairs. Zoom-in images of the line pairs from resolvable to irresolvable are provided at the lower-left corner of each image. Figure 6 shows 1D profiles that pass through the centers of the line pairs indicated by dashed white arcs in Fig. 5. With β values properly chosen, the proposed method is able to significantly reduce the noise of the reconstructed image with a negligible resolution loss.

For a quantitative analysis of the image quality, another scan was carried out on the Catphan©600 phantom without the oval body annulus. A narrow collimator was used to further reduce the scatter. The reconstructed image, as shown in Fig. 7, is considered as a benchmark image. Seven ROIs as indicated in Fig. 7 are used to calculate the contrasts, and the results are summarized in Table I. The error relative to the contrasts of the benchmark image is provided in parentheses. The scatter correction greatly reduces the reconstruction errors. The average reconstruction error is reduced from 65.9% to 10.6% when the scatter correction is applied. Using the proposed noise suppression algorithm, the average error is further reduced to 5.8% when a small β is used and 1.7% when a large β is used. The comparison also shows that when the image resolution is matched, the proposed algorithm is superior to the standard method using a Hamming filter and the previously developed PWLS algorithm.

Table II shows the CNRs for different ROIs. After scatter correction, although the reconstruction error is greatly reduced and image contrast is increased, the average CNR de-

TABLE II. CNR comparison of the selected ROIs.

ROI	1	2	3	4	5	6	7	Average
No scatter correction [Fig. 1(a)]	1.37	4.57	6.57	1.68	1.28	0.74	5.78	3.14
Scatter correction only [Fig. 1(b)]	1.29	3.94	5.58	1.15	0.99	0.38	4.54	2.55
Proposed algorithm, β=0.0009 [Fig. 1(c)]	4.12	14.16	17.14	4.87	3.28	2.09	18.47	9.16
Proposed algorithm, β=0.0001 [Fig. 1(d)]	1.86	6.07	8.37	2.08	1.57	0.74	8.02	4.10
Using a Hamming filter [Fig. 1(e)]	1.60	4.90	6.86	1.42	1.21	0.57	5.81	3.19
Proposed algorithm, s_e=0 [Fig. 1(f)]	1.58	4.97	6.98	1.43	1.14	0.48	5.59	3.17

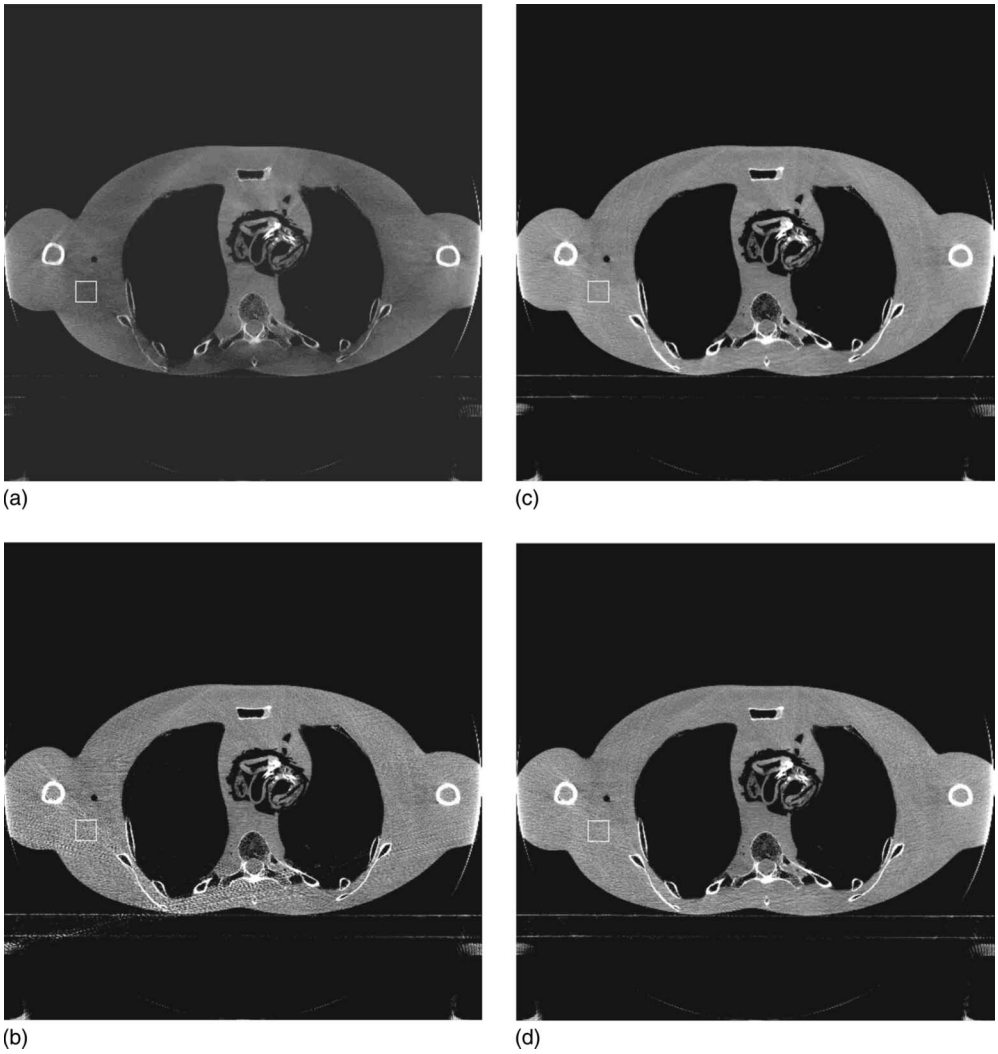

FIG. 8. Reconstructed images of the anthropomorphic phantom. Display window: [−500 500] HU. The mean and standard deviation (std) inside the white squares in the images are measured as mean ± std HU. (a) No scatter correction and no noise suppression; CT number in the selected ROI (white square): −291 ± 43 HU. (b) Scatter correction without noise suppression; CT number in the selected ROI: 1 ± 146 HU. (c) Scatter correction using the proposed noise suppression algorithm, β=0.001; CT number in the selected ROI: 17 ± 46 HU. (d) Scatter correction using the proposed noise suppression algorithm, β =0.0001; CT number in the selected ROI: 18 ± 89 HU.

creases from 3.14 to 2.55 due to the image noise magnification. Using the proposed noise suppression algorithm, the average CNR increases to 4.10 for a small β and 9.16 for a large β.

Figure 8 shows the reconstruction results of the anthropomorphic phantom. Note that a bowtie filter was used in the scan, which made the SPR more uniform. However, along the projection lines which pass through highly attenuating objects, such as bones, the SPR can still be very high (around 8) due to the extremely low primary signals. After the logarithm operation, the noise in those projection data boosts up after an effective scatter correction and results in streaking artifacts in the reconstruction, which is obvious in Fig. 8(b). As shown in Figs. 8(c) and 8(d), these artifacts are effectively suppressed using the proposed algorithm, and the image noise is also reduced. Figure 9 shows the difference images before and after the proposed noise suppression. Figure 10 compares 1D central vertical profiles of the images shown in Fig. 8.

IV. DISCUSSION

Majority of the existing scatter correction methods use postprocessing techniques on the scatter contaminated projection images to improve the reconstruction accuracy. These methods only partially solve the problem caused by scatter and leave the high frequency components of the scatter signal intact, which often leads to degraded CNRs and image quality. In this work, both theoretical analysis and physical experiments show the effect of noise magnification in the reconstructed image due to scatter correction. Experiments were carried out on a clinical CBCT system with a commonly used protocol on phantoms with a human size. The

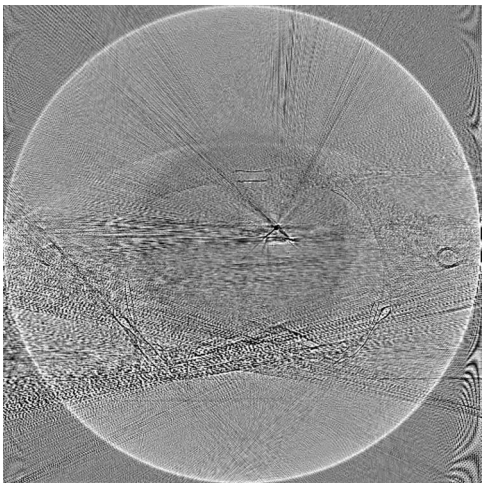

(a)

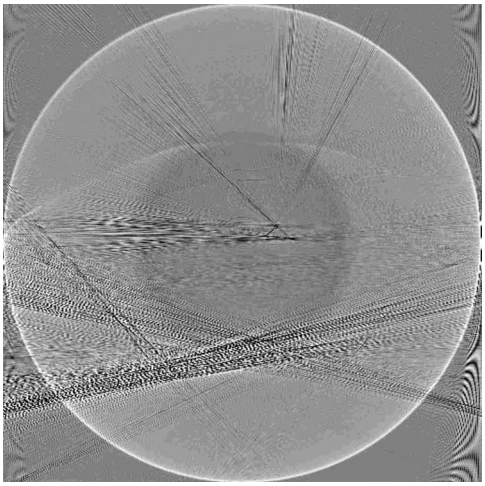

(b)

FIG. 9. Difference images after applying noise suppression on Fig. 8(b) using different algorithm parameters. Display window: [−150 150] HU. (a) Scatter correction using the proposed noise suppression algorithm, β = 0.001 [Fig. 8(c)– Fig. 8(b)]. (b) Scatter correction using the proposed noise suppression algorithm, β = 0.0001. [Fig. 8(d)–Fig. 8(b)].

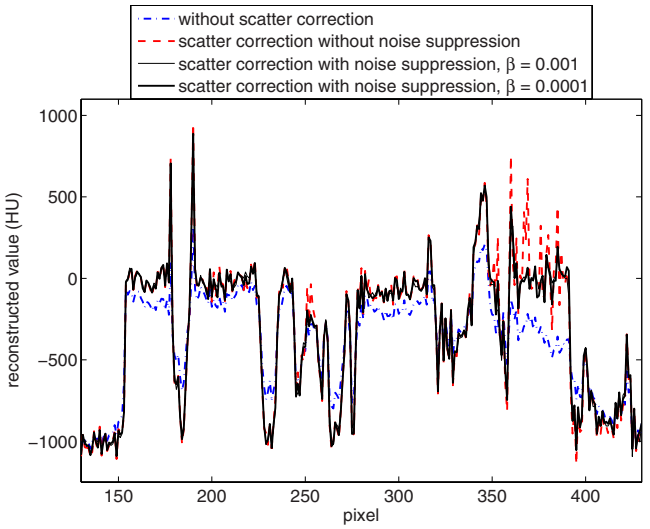

FIG. 10. Comparison of 1D central vertical profiles of the images shown in Fig. 8. The results using the proposed noise suppression algorithm with different β values have a relatively large difference only in the noisy areas.

results indicate that an effective scatter correction alone does not provide satisfactory images in CBCT because the gain from the scatter reduction is inevitably accompanied with overwhelming noise-related artifacts. One traditional method to deal with the noise problem is to increase the dose. However, the results on both the evaluation phantom and the anthropomorphic phantom show that the noise variance increases by a factor of more than 10 when scatter correction is applied. Since noise variance of a CT image is roughly inversely proportional to the total number of incident photons,[24] the dose needs to be increased by a factor of more than 10 in order to make the noise level of the scatter corrected image comparable to that without scatter correction. This excessive dose increase is hardly acceptable in clinical practice.[25]

An improved PWLS algorithm is implemented in this work to suppress the noise in reconstructed images. The PWLS objective function models the first-order and second-order statistics of the measurements and it is equivalent to the penalized maximum likelihood (pML) or maximum a posteriori (MAP) criterion for the independent Gaussian distributed noise. Indeed, the noise of CT line integrals can be well approximated by Gaussian noise based on an experimental study.[26] Therefore, the minimization of the PWLS objective function gives an optimal solution in a statistical sense. In the previous work, we have shown that the performance of the PWLS algorithm is better than those low-pass filters during image reconstruction or noise reduction filters based on local statistics of measurements.[17] In this paper, both results on the evaluation phantom and the anthropomorphic phantom show effective reduction in global image noise as well as local streaking artifacts around high attenuating objects, such as bones. While a measurement-based scatter correction method is used to demonstrate the nature of the noise magnification problem incurring in the process of scatter removal, the developed noise suppression algorithm is expected to work effectively with other scatter correction algorithms as long as they can provide accurate scatter estimates.

One concern about a noise suppression algorithm is the possible resolution loss due to smoothing. We compare the proposed algorithm with the standard noise suppression method using a Hamming filter on the projection images. The comparison shows that when a similar image resolution is achieved, the proposed algorithm is superior on noise suppression. Our results also show that using a conservative smoothing strategy, significant noise reduction is still achievable with negligible resolution loss. The choice of parameter β in the PWLS algorithm is a tradeoff between reconstruction accuracy and resolution loss. In adaptive radiation therapy using CBCT, for example, the CBCT images are used for dose calculation and the CT number accuracy is

more important than the image resolution. In such an application, an aggressive noise suppression strategy (a large β) should be used.

The proposed algorithm is based on the previously developed PWLS algorithm. To show the significance of including the scatter estimate s_e in the the noise estimation formula [Eq. (11)], we compare the results using the proposed new algorithm and the previously developed PWLS algorithm. The latter is equivalent to the proposed algorithm with a zero scatter estimate. Similar to the comparison with the result using Hamming filtering, the proposed algorithm achieves lower noise when the same image resolution is maintained. Note that this degraded ability of noise suppression using the previously developed PWLS algorithm is not due to the underestimation of total noise magnitude by assuming zero scatter signals, since such an underestimation can always be compensated for using a larger β in the algorithm. The essence of the PWLS algorithms is to equalize the noise variance of different pixels by assigning different weights. The presence of scatter greatly changes the spatial distribution of the noise variance. Since the noise variance is proportional to $(1+SPR)^2$ according to Eq. (10), and SPR spatially varies from values close to zero to those larger than 8, the true spatial distribution of the noise variance is quite different from that if the scatter is assumed to be zero. The misestimation of scatter results in incorrect estimation of noise spatial distribution, and the corresponding weighting in the PWLS algorithm is not able to equalize the noise variance of each projection pixel. The noise suppression ability is therefore significantly compromised. To illustrate the importance of accurate scatter estimation for a superior noise suppression performance, we also compare the result using the proposed algorithm with a uniform scatter estimate. Since uniform scatter estimation results in an estimate of SPR distribution much less accurate than that using a zero scatter estimate, the noise suppression performance is also much worse. Finally, we want to emphasize that the inaccuracy in scatter estimation compromises the performance of noise suppression using the proposed method, however, it does not make reconstruction less accurate than that without noise suppression. We can always tune the β value based on the tradeoff between the noise suppression capability and the image artifacts caused by inaccurate scatter estimation.

V. CONCLUSION

Scatter correction methods based on postprocessing fall short in eliminating the high-frequency scatter noise and are incapable of providing satisfactory CBCT image quality. Using a clinical CBCT system with conventional imaging settings, we have shown that after scatter correction, the noise variance in selected ROIs of the reconstructed image can be increased by a factor of more than 10. We argue that a scatter correction algorithm should be used together with a noise suppression algorithm to achieve a satisfactory image. A PWLS algorithm is proposed for the noise suppression. The phantom experiments indicate that the algorithm is able to further reduce the reconstruction error in a scatter corrected image without noise suppression from 10.6% to 1.7%, and the average CNR in selected ROIs is also increased by a factor of 3.6. The improvement in image quality is critical in many clinical applications of CBCT, such as accurate dose calculation and tumor target delineation in radiation therapy planning.

ACKNOWLEDGMENTS

This project was supported in part by grants from Department of Defense (W81XWH-08-1-0127), Komen Foundation (BCTR 0504071) and National Cancer Institute (1R01 CA98523 and CA104205). The authors also thank Triple Ring Technology for providing the anthropomorphic phantom.

[a]Electronic mail: leizhu@stanford.edu

[1]G. H. Glover, "Compton scatter effects in CT reconstructions," Med. Phys. **9**, 860 (1982).
[2]P. M. Joseph and R. D. Spital, "The effects of scatter in x-ray computed tomography," Med. Phys. **9**, 464 (1982).
[3]T. R. Fox, D. T. Nisius, H. Aradate, and Y. Saito, "Practical x-ray scatter measurements for volume CT detector design," Proc. SPIE **4320**, 808 (2001).
[4]L. Zhu, N. R. Bennett, and R. Fahrig, "Scatter correction method for x-ray CT using primary modulation: theory and preliminary results," IEEE Trans. Med. Imaging **25**, 1573 (2006).
[5]R. Ning, X. Tang, and D. Conover, "X-ray scatter correction algorithm for cone beam CT imaging," Med. Phys. **31**, 1195 (2004).
[6]J. H. Siewerdsen, M. J. Daly, B. Bakhtiar, D. J. Moseley, S. Richard, H. Keller, and D. A. Jaffray, "A simple, direct method for x-ray scatter estimation and correction in digital radiography and cone-beam CT," Med. Phys. **33**, 187 (2006).
[7]G. Jarry, S. A. Graham, D. J. Moseley, D. J. Jaffray, J. H. Siewerdsen, and F. Verhaegen, "Characterization of scattered radiation in kV CBCT images using Monte Carlo simulations," Med. Phys. **33**, 4320 (2006).
[8]J. Rinkel, L. Gerfault, F. Estve, and J.-M. Dinten, "A new method for x-ray scatter correction: first assessment on a cone-beam CT experimental setup," Phys. Med. Biol. **52**, 4633 (2007).
[9]Y. Kyriakou, T. Riedel, and W. A. Kalender, "Combining deterministic and Monte Carlo calculations for fast estimation of scatter intensities in CT," Phys. Med. Biol. **51**, 4567 (2006).
[10]J. Persliden and G. A. Carlsson, "Scatter rejection by air gaps in diagnostic radiology calculations using a monte carlo collision density method and consideration of molecular interference in coherent scattering," Phys. Med. Biol. **42**, 155 (1997).
[11]J. H. Siewerdsen, D. J. Moseley, B. Bakhtiar, S. Richard, and D. A. Jaffray, "The influence of antiscatter grids on soft-tissue detectability in cone-beam computed tomography with flat-panel detectors," Med. Phys. **31**, 3506 (2004).
[12]Y. Kyriakou and W. Kalender, "Efficiency of antiscatter grids for flat-detector CT," Phys. Med. Biol. **52**, 6275 (2007).
[13]J. Y. Lo, C. E. Floyd, J. A. Baker, and C. E. Ravin, "Scatter compensation in digital chest radiography using the posterior beam stop technique," Med. Phys. **21**, 435 (1994).
[14]J. A. Seibert and J. M. Boone, "X-ray scatter removal by deconvolution," Med. Phys. **15**, 567 (1988).
[15]M. Honda, K. Kikuchi, and K. Komatsu, "Method for estimating the intensity of scattered radiation using a scatter generation model," Med. Phys. **18**, 219 (1991).
[16]K. J. Engel, C. Herrmann, and G. Zeitler, "X-ray scattering in single- and dual-source CT," Med. Phys. **35**, 318 (2008).
[17]J. Wang, T. Li, H. Lu, and Z. Liang, "Penalized weighted least-squares approach to sinogram noise reduction and image reconstruction for low-dose x-ray computed tomography," IEEE Trans. Med. Imaging **25**, 1272 (2006).
[18]A. C. Kak and M. Slaney, *Principles of Computerized Tomography* (IEEE, Piscataway, NJ, 1987).
[19]J. Boone and J. Seibert, "An analytical model of the scattered radiation

distribution in diagnosticradiology," Med. Phys. **15**, 721 (1998).
[20]J. Wang, T. Li, H. Lu, and Z. Liang, "Noise reduction for low-dose single-slice helical CT sinograms," IEEE Trans. Nucl. Sci. **53**, 1230 (2006).
[21]J. Wang, T. Li, Z. Liang, and L. Xing, "Dose reduction for kilovoltage cone-beam computed tomography in radiation therapy," Phys. Med. Biol. **53**, 2897 (2008).
[22]P. Perona and J. Malik, "Scale-space and edge detection using anisotropic diffusion," IEEE Trans. Pattern Anal. Mach. Intell. **12**, 629 (1990).
[23]L. A. Feldkamp, L. C. Davis, and J. W. Kress, "Practical cone-beam algorithm," J. Opt. Soc. Am. **1**, 612 (1984).
[24]S. J. Riederer, N. J. Pelc, and D. A. Chesler, "The noise power spectrum in computed x-ray tomography," Phys. Med. Biol. **23**, 446 (1978).
[25]D. J. Brenner and E. J. Hall, "Computed tomography—an increasing source of radiation exposure," N. Engl. J. Med. **357**, 2277 (2007).
[26]J. Wang, H. Lu, D. Eremina, G. Zhang, S. Wang, J. Chen, J. Manzione, and Z. Liang, "An experimental study on the noise properties of x-ray CT sinogram data in the radon space," Phys. Med. Biol. **53**, 3327 (2008).

Int. J. Radiation Oncology Biol. Phys., Vol. ■, No. ■, pp. 1–7, 2009

0360-3016/09/$–see front matter

ELSEVIER

doi:10.1016/j.ijrobp.2009.01.020

PHYSICS CONTRIBUTION

NOISE REDUCTION IN LOW-DOSE X-RAY FLUOROSCOPY FOR IMAGE-GUIDED RADIATION THERAPY

JING WANG, PH.D., LEI ZHU, PH.D., AND LEI XING, PH.D.

Department of Radiation Oncology, Stanford University School of Medicine, Stanford, CA

Purpose: To improve the quality of low-dose X-ray fluoroscopic images using statistics-based restoration algorithm so that the patient fluoroscopy can be performed with reduced radiation dose.

Method and Materials: Noise in the low-dose fluoroscopy was suppressed by temporal and spatial filtering. The temporal correlation among neighboring frames was considered by the Karhunen-Loève (KL) transform (*i.e.*, principal component analysis). After the KL transform, the selected neighboring frames of fluoroscopy were decomposed to uncorrelated and ordered principal components. For each KL component, a penalized weighted least-squares (PWLS) objective function was constructed to restore the ideal image. The penalty was chosen as anisotropic quadratic, and the penalty parameter in each KL component was inversely proportional to its corresponding eigenvalue. Smaller KL eigenvalue is associated with the KL component of lower signal-to-noise ratio (SNR), and a larger penalty parameter should be used for such KL component. The low-dose fluoroscopic images were acquired using a Varian Acuity simulator. A quality assurance phantom and an anthropomorphic chest phantom were used to evaluate the presented algorithm.

Results: In the images restored by the proposed KL domain PWLS algorithm, noise is greatly suppressed, whereas fine structures are well preserved. Average improvement rate of SNR is 75% among selected regions of interest. Comparison studies with traditional techniques, such as the mean and median filters, show that the proposed algorithm is advantageous in terms of structure preservation.

Conclusions: The proposed noise reduction algorithm can significantly improve the quality of low-dose X-ray fluoroscopic image and allows for dose reduction in X-ray fluoroscopy.

Low-dose fluoroscopy, Penalized weighted least-squares, Karhunen-Loève (KL) transform, Noise reduction, Anisotropic penalty.

INTRODUCTION

X-ray fluoroscopic imaging plays an important role in image-guided radiation therapy (IGRT). There is growing interest in using X-ray fluoroscopy for the management of organ motion and gating in radiotherapy (1–4). Both room-mounted orthogonal X-ray fluoroscopic imaging system (2) and gantry-mounted fluoroscopy (3) have been developed for tumor tracking and gating for radiotherapy. Recently, a method for real-time tracking of implanted fiducial marker was developed using combination of kV and MV imaging (4). The X-ray fluoroscopic imaging provides additional information of tumor and patient structure; however, it is not risk-free. The extra exposure to X-rays during fluoroscopy may lead to adverse health effects in patients. Therefore, low-dose fluoroscopic imaging is desirable in clinics.

Low-dose fluoroscopy can be achieved using a lower mA and pulse length during acquisition images (5). With a lower mAs acquisition protocol, the image quality will be degraded because of excessive photon quantum noise. Several spatial and temporal noise reduction algorithms (6–11) have been studied to remove signal-dependent noise in the low-dose fluoroscopic images. Temporal filtering techniques incorporate information from neighboring frames and can potentially improve the performance of two-dimensional (2D) spatial filtering. However, temporal filters could introduce motion artifacts in the filtered fluoroscopic images if motion in the fluoroscopy is not handled properly. One way to avoid motion artifacts resulting from temporal filters is to estimate the motion information from the fluoroscopic image sequences and compensate for it during filtering process. Nevertheless, estimation of motion fields from 2D image sequences is challenging because of its ill-posed nature and excessive noise (12–14). In this work, we aimed to reduce noise at low doses through improved temporal filtering and

Reprint requests to: Department of Radiation Oncology, Stanford University School of Medicine, 875 Blake Wilbur Drive, Stanford, CA 94305-5847. Tel: (650) 723-4496; Fax: (650) 498-4015; E-mail: jingwang9@stanford.edu

This work was support in part by grants from the Department of Defense (Grant Nos. W81XWH-08-1-0127 and W81XWH-05-1-0041) and National Cancer Institute (Grant Nos. 1R01 CA98523 and CA104205).

Conflicts of interest: none.

Received May 23, 2008, and in revised form Nov 26, 2008. Accepted for publication Jan 9, 2009.

statistics-based image restoration. Instead of estimating explicit motion fields from 2D image sequences, we considered the correlation between neighboring frames of fluoroscopy by using the Karhunen-Loève (KL) transform. The KL transform has been proved to be useful in image restoration (15) and tomographic image reconstruction (16, 17). The KL transform considers similarities as well as differences between neighboring frames. For each KL component, the noise was reduced according to the penalized weighted least-squares (PWLS) criterion. The presented method was evaluated using two phantom experimental studies.

METHODS AND MATERIALS

In this section, we first introduce the PWLS criterion for spatial noise filtering. We then describe the KL transform for temporal filtering, followed by the summary of the implementation of the KL domain PWLS algorithm. We later describe the data acquisition of two experimental studies.

Spatial filtering using the PWLS criterion

Mathematically, the PWLS objective function can be described by the following equation:

$$\Phi(u) = (\hat{y} - \hat{u})^T \sum^{-1} (\hat{y} - \hat{u}) + \beta R(u). \quad (1)$$

The first term in Eq. 1 is a weighted least-squares (WLS) criterion, where $\hat{y}$ is the vector of the measured data and $\hat{u}$ is the vector of ideal fluoroscopy to be estimated. T denotes the transpose operator. The matrix $\sum$ is the covariance matrix of $\hat{y}$ and its ith diagonal element $\sigma^2 i$ is the variance of measured data at detector bin i; it determines the contribution of each measurement to the objective function because it plays the weighting role in the WLS criterion. The variance of each measurement can be estimated from the mean-variance relationship of Fig. 1. To obtain the mean-variance relationship of low-dose fluoroscopic images, 600 repeated fluoroscopic images of the anthropomorphic chest phantom were acquired when the platform was static. Mean and variance of each pixel were then calculated from repeated measurements and plotted in Fig. 1. It can be observed that mean and variance of measured data are linear, which reflects the Poisson noise nature of X-ray photons. A non-zero intersect can also be observed and is caused by background electronic noise.

The second term in Eq. 1 is a smoothness penalty or *a priori* constraint, where β is the smoothing parameter that controls the degree of agreement between the estimated and the measured data. A commonly used penalty is a quadratic term (17, 18):

$$R(\mu) = \mu' R \mu = \frac{1}{2} \sum_j \sum_{m \in N_j} k_{jm} (\mu_j - \mu_m)^2, \quad (2)$$

where index j runs over all elements in the fluoroscopic image, and N_j represents the set of neighbors of the j-th pixel. The parameter k_{jm} indicates the relative contribution of different neighbors and is usually set to 1 for first-order neighbors and $1/\sqrt{2}$ for second-order neighbors. One drawback of this choice is that it considers only distance information of neighbors to regularize the solution and may lead to oversmoothing in the restored image, especially around sharp edges. To avoid oversmoothing around edges, we chose an edge-preserving penalty (19) by incorporating the gradient information into the parameter k_{jm}. The weight can be written as:

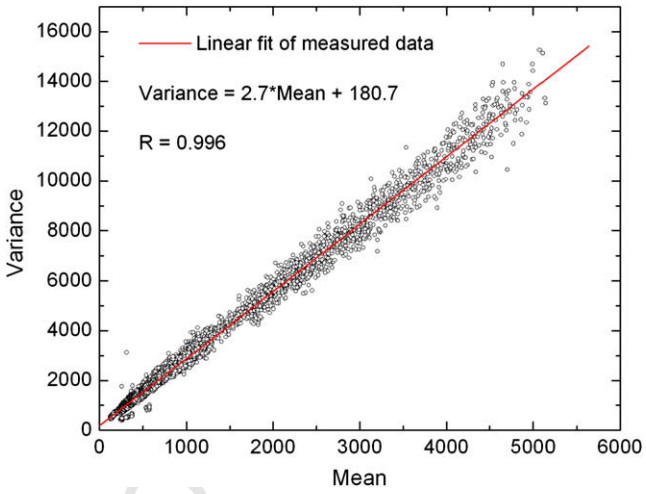

Fig. 1. Linear relationship between mean and variance of X-ray fluoroscopic image.

$$k'_{jm} = k_{jm} \exp\left[- \left(\frac{\mu_j - \mu_m}{\delta} \right)^2 \right]. \quad (3)$$

This new parameter has a form similar to the anisotropic diffusion filter (20), in which the gradient and the parameter δ determines the strength of diffusion during each iteration. The parameter δ provides local control of smoothness and can be chosen as a value such that 90% of the pixels in the image to be processed have a gradient magnitude smaller than δ. The parameter k'_{jm} is small if the gradient between the neighbor and the concerned pixel is large. The neighbors with large gradient usually occur at the edges, and equivalence between such neighbors is discouraged by introducing Eq. 3. Therefore, the edges will be better preserved in the de-noised image.

The minimization of the PWLS objective function (1) can be performed efficiently using Gauss-Seidel updating strategy (21):

$$u_i^{(n+1)} = \frac{y_i + \beta \sigma_i^2 \left(\sum_{m \in N_i^1} k'_{im} u_m^{(n+1)} + \sum_{m \in N_i^2} k'_{im} u_m^{(n)} \right)}{1 + \beta w_i \sum_{m \in N_i} k_{im}}, \quad (4)$$

where index n represents iterative number, N_i^1 denotes the two nearest neighbors of i in which the index is smaller than i, N_i^2 denotes those two nearest neighbors of i in which the index is larger than i, and N_i denotes these four nearest neighbors of pixel i in the fluoroscopic image. The initial of $\hat{u}$ is given by the measured data $\hat{y}$.

Temporal filtering using the KL transform

In fluoroscopy, different image frames are highly correlated for the same patient, especially among neighboring frames. One way to use the correlation among neighboring frames is the KL transform (KLT). Following KLT, the selected neighboring fluoroscopy frames were decomposed to uncorrelated and ordered principal components. Each KL component was associated with an eigenvalue, which can be effectively used during spatial filtering of fluoroscopic imaging. In this work, two frames of the image preceding the frame under consideration were chosen to perform KLT. This selection of neighboring frames is based on idea that only previously obtained frames are available to process the chosen frame in real time. The KL transform is defined as:

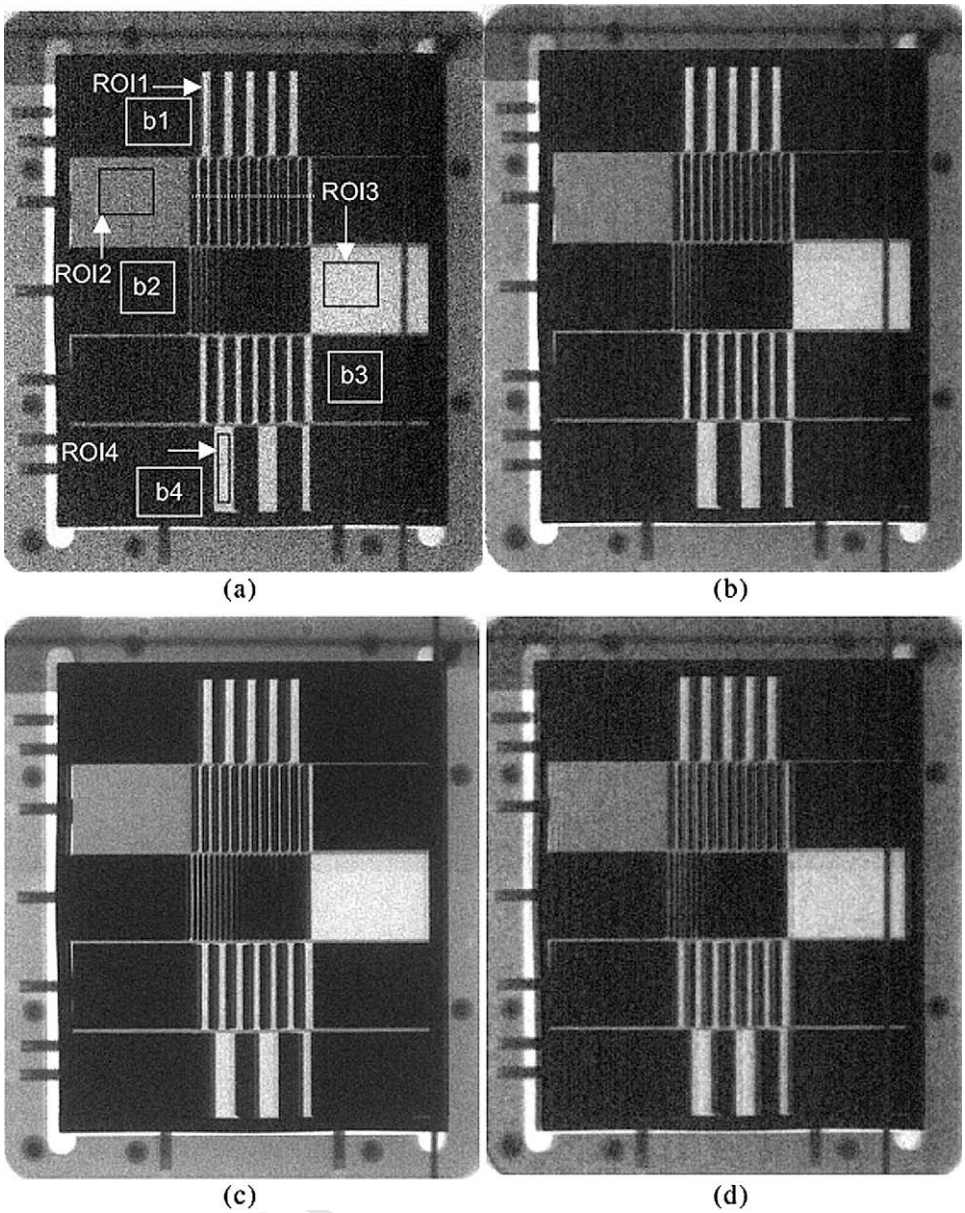

Fig. 2. Fluoroscopic image of the quality assurance phantom: (a) acquired with X-ray tube current 10 mA and pulse length 2 ms; (b) image (a) processed by the Karhunen-Loève (KL) domain penalized weighted least-squares (PWLS) noise reduction algorithm; (c) acquired with X-ray tube current 10 mA and pulse length 10 ms. (d) Image in panel a processed with the KL domain PWLS using an isotropic quadratic term as a penalty. In panel a, b1, b2, b3, and b4 indicate the background region for the calculation of signal-to-noise ratios. Blurred edges can be observed in panel d. ROI = region of interest.

$$\tilde{y} = A\hat{y}, \tag{5}$$

where $\hat{y}$ is vector of selected frames of fluoroscopy and is arranged in a such way that each row comprised one frame of the fluoroscopic image. $\tilde{y}$ is the KL-transformed fluoroscopic image, and A is the KLT matrix that can be calculated from $\hat{y}$. From the selected frames of fluoroscopy $\hat{y}$, the elements of the covariance matrix K_t can be calculated by:

$$[k_t]_{kl} = \frac{1}{B-1}\sum_{i=1}^{B}\left(y_{i,k} - \bar{y}_k\right)\left(y_{i,l} - \bar{y}_l\right), \tag{6}$$

where $y_{i,k}$ is the datum of fluoroscopy $\hat{y}$ at detector bin i of *k-th frame*, $y_{i,l}$ is the datum of $\hat{y}$ at detector bin i of *l-th frame*. $\overline{y_k}$ and $\overline{y_l}$ are the mean of fluoroscopic image of k-th frame and l-th frame respectively. B is the number of detector bins for each fluoroscopy and index k or l runs over the selected nearby frames. From the covariance matrix K_t, the KLT matrix A can then be calculated based on

$$K_t A' = A' D. \tag{7}$$

In Eq. 7, $D = diag\{d_l\}_{l=1}^{3}$, where d_l is the l-th eigenvalue of K_t. After the KLT, the covariance $\tilde{K}_t$ of $\tilde{y}$ will be:

$$\tilde{K}_t = AK_tA' = diag\{d_l\}_{l=1}^{3}. \tag{8}$$

Equation 8 implies that the covariance matrix of the KL-transformed data is diagonal, that is, the covariance of the signal between different frames after the KLT will be zero. Therefore, the data signals of different KL components are no longer correlated so that

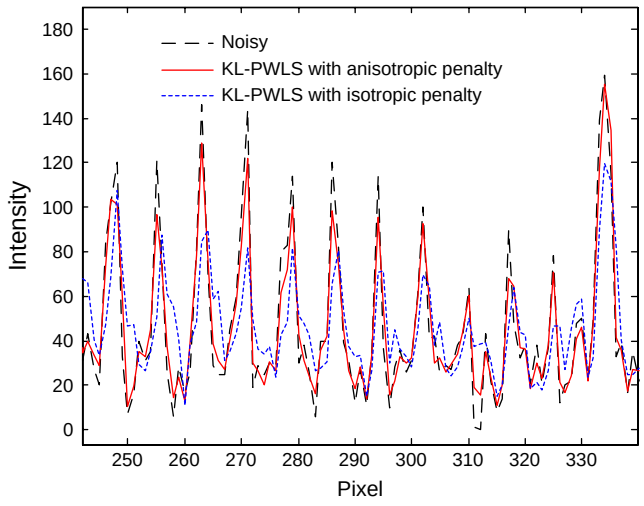

Fig. 3. Profiles across the bars in Fig. 2 (indicated by a dashed line in Fig. 2a). KL = Karhunen-Loève; PWLS = penalized weighted least-squares.

PWLS objective function can be constructed for each KL principal component separately. For each principal component in the KL domain, the PWLS cost function can be expressed as (16–18):

$$\Phi_l(\tilde{u}_l) = (\tilde{y}_l - \tilde{u}_l)' \tilde{\sum}_l^{-1} (\tilde{y}_l - \tilde{u}_l) + (\beta/d_l)\tilde{R}(\tilde{u}_l), \qquad (9)$$

where $\tilde{y}_l$ and $\tilde{u}_l$ are the l-th KL components of $\hat{y}$ and u respectively, and $\tilde{\sum}_l$ is the diagonal weighting matrix of in the KL domain which can be estimated by:

$$\tilde{\sum}_l = diag\{\varphi_l' Q_i \varphi_l\}_{i=1}^{b}, \qquad (10)$$

where $Q_i = diag\{\sigma_{i,k}^2\}_{k=1}^{3}$ is the variance matrix of the projection at bin i, $\sigma_{i,k}^2$ is the variance of $y_{i,k}$, and φ_l is the l-th KL basis vector. $\tilde{R}(\tilde{u}_l)$ is the edge-preserving penalty term which can be defined as:

$$\tilde{R}(\tilde{u}_l) = \tilde{u}_l' \tilde{R} \tilde{u}_l = \frac{1}{2} \sum_i \sum_{m \in N_i} k_{im}' (\tilde{u}_{i,l} - \tilde{u}_{m,l})^2 \qquad (11)$$

Equation 9 shows that the smoothing parameter in the KL domain shall be chosen as (β/d_l), and the PWLS criterion for each KL component becomes adaptive to its corresponding eigenvalue. This choice is favorable because the smoothing parameter varies adaptively according to the signal-to-noise ratio (SNR) of that component. A smaller KL eigenvalue is usually associated with a component having a lower SNR (16) and, therefore, a larger smoothing parameter is used to penalize this noisier data component.

In summary, implementation of the presented KL domain PWLS noise reduction approach for the low-dose fluoroscopy can be described as follows:

1. For a j-th frame fluoroscopic image, the (j-1)-th and the (j-2)-th frame of the images are selected for the KL transform.
2. Compute the covariance matrix k_t from the selected frames of the projections.
3. Calculate the KL transform matrix A according to Eq. 7.
4. Apply the KL transform on the selected frames of fluoroscopic images.
5. Perform PWLS minimization on each KL component.
6. Apply inverse KL transform on the processed KL components for the estimate of the ideal fluoroscopy at the chosen j-th frame.

Table 1. SNRs of different ROIs in figure 2.

	ROI1	ROI2	ROI3	ROI4
10 ms	9.7	10.5	14.3	9.9
2 ms	5.8	3.8	6.2	5.3
KL domain PWLS 2 ms β= 200	8.3	7.9	12.8	7.5

Abbreviations: KL = Karhunen-Loève; PWLS = penalized weighted least-squares; ROI = region of interest.

Data acquisition

The X-ray fluoroscopic images were acquired using an Acuity simulator (Varian Medical Systems, Palo Alto, CA). The dimension of the sensitive area of the detector is 397 mm × 298 mm, containing 1024 × 768 pixels. Two phantoms were used to evaluate the presented KLT and PWLS-based noise reduction algorithm. The first phantom was a commercial quality assurance phantom, in which several fine strips can be used to evaluate the fine structure preservation of the algorithm. The second phantom was an anthropomorphic chest phantom. To simulate the respiratory motion of patients, each phantom was placed on the top of a platform capable of sinusoidal motion in the cranial-caudal direction. The amplitude of motion of the platform was 3.5 cm, and the period of motion was set at 3 s. The selected motion parameters correspond to those of a patient with large respiratory motion and fast breathing (22). In both phantom studies, the X-ray tube current was set at 10 mA, and the pulse length of X-ray was 2 ms for low-dose and 10 ms for high-dose fluoroscopic image. The acquisition frame rate was 5 frames per second, and all sequences consisted of 20 frames.

RESULTS

Quality assurance phantom

We first tested the presented algorithm on the quality assurance (QA) phantom placed on the moving platform. The QA phantom contains several fine strips that can be used to study the edge information in the processed images. Figure 2a shows one frame of fluoroscopic images obtained with X-ray tube current 10 mA and duration of X-ray pulse length 2 ms. Figure 2b shows the same frame of image processed by the presented KL domain PWLS noise reduction algorithm. It can be observed that noise in the low-dose fluoroscopic image is greatly suppressed, and the image is comparable to that obtained with the 10-ms protocol (Fig. 2c). One challenge for temporal filtration of fluoroscopic images is that tailing artifacts may be presented in the motion portion of the processed image (23). It can be observed in Fig. 2b that the fine strips are well-preserved, and no tailing artifacts have been introduced by the temporal filtering using the KL transform. However, if the isotropic quadratic term was used as the penalty term in the PWLS objective function, the edges in the processed fluoroscopic images could be blurred. Figure 2d shows the image processed by KL domain PWLS with isotropic quadratic penalty. It can be observed that the fine structures have been severely blurred. Profiles through the fine strips, as shown in Fig. 3, further illustrate these observations. Those results suggest that the edge-preserving penalty is desired in the PWLS objective function.

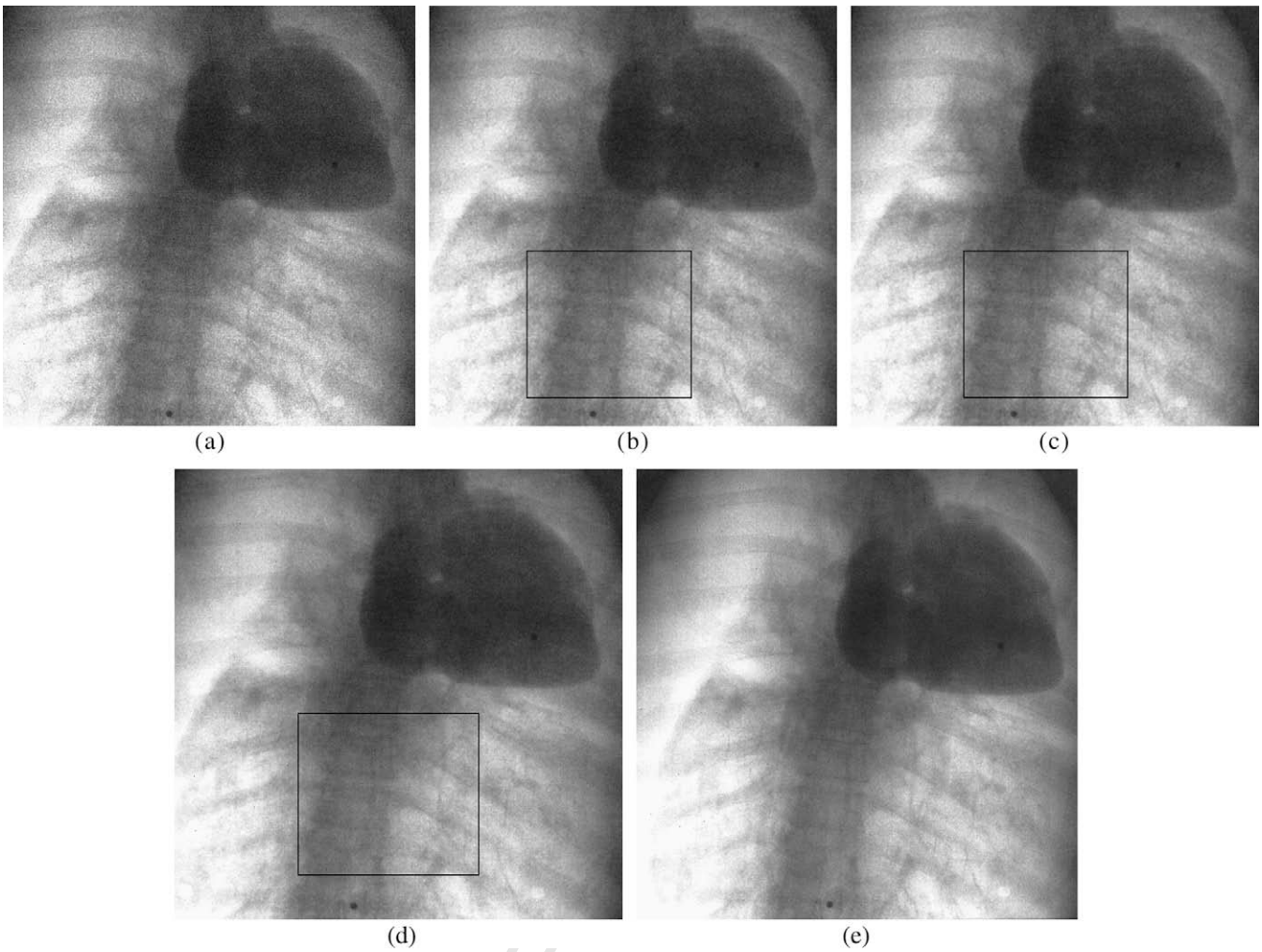

Fig. 4. Fluoroscopic image of the anthropomorphic chest phantom. (a) Acquired with tube current 10 mA and pulse length 2 ms; (b) image in panel a processed by with the two-dimensional (2D) mean filter; (c) image in panel a processed with the 2D median filter; (d) image in panel a processed by the Karhunen-Loève KL domain penalized weighted least-squares noise reduction algorithm; and (e) image acquired with tube current 10 mA and pulse length 10 ms.

To evaluate the effectiveness of the presented algorithm quantitatively, SNR of different regions of interest (ROIs) was calculated. The SNR is defined as:

$$SNR = \frac{|u_s - u_b|}{\sigma_s}, \tag{12}$$

where u_s is the mean value the signal, u_b is the mean value of background (a uniform region nearby the selected ROI), and σ_s is the standard deviation of the signal. Four regions (indicated by arrows in Fig. 2a) were chosen to calculate SNRs, and the results are presented in Table 1. The improvement of the SNRs in the image after the KL domain PWLS processing varies according to the locations. The range of improvement in SNRs is between 41% and 108%, and the average improvement is 75% among the four chosen ROIs.

Anthropomorphic chest phantom

Results of the anthropomorphic chest are shown in Fig. 4. Figure 4a shows one frame of fluoroscopic images obtained with 2-ms pulse length protocol. Figure 4d shows the image processed by the KL domain PWLS noise reduction algorithm. It can be observed that the noise is greatly suppressed, whereas the fine structures are well preserved. Figure 5 provides the difference image between Fig. 4a and 4d, in which random noise is dominant and no edges or structures can be observed. This indicates that good edge preservation can be achieved by the KL domain PWLS noise reduction algorithm. It can also be observed that the processed image obtained with the 2-ms protocol is comparable to that obtained with a 10-ms protocol (see Fig. 4e). We also compared the presented algorithm with conventional filters such as the mean and median filter. Figure 4b shows the corresponding frame processed by the mean filter with a 3×3 window. Figure 4c shows the result from the median filter with a 3×3 window. It can be observed that the image quality of the KL domain PWLS processed image is superior to those images processed by the mean and median filter from the bony structures indicated by the rectangular square in Fig. 4b–4d.

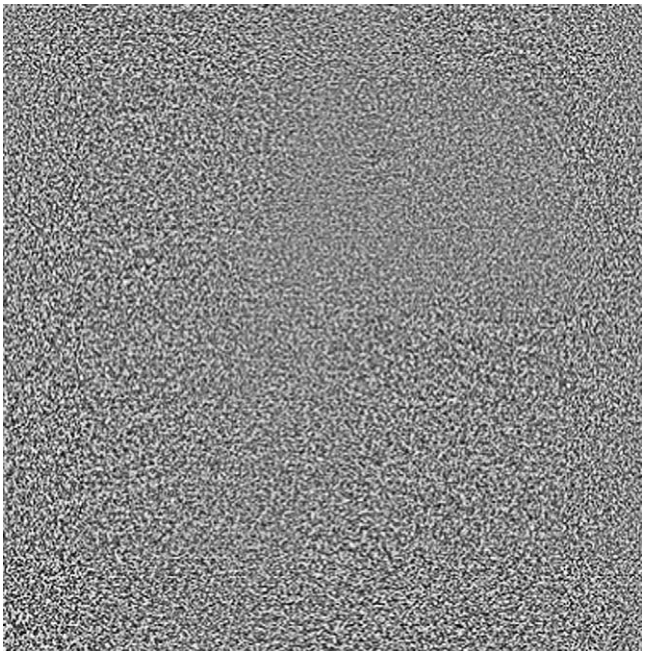

Fig. 5. Difference image of the chest phantom between the Karhunen-Loève domain penalized weighted least-squares processed image (Fig. 4d) and the noisy low-dose image (Fig. 4a).

DISCUSSION

In this work, we proposed a temporal-spatial filter to reduce noise in low-dose X-ray fluoroscopy. The KL transform was used to account for correlation among neighboring frames of fluoroscopic imaging. The explicit estimation of motion fields are avoided during the de-noising process. The KLT decomposes the correlated image sequences into uncorrelated KL components. Following KLT, the PWLS criterion is used to restore each KL component, and the smoothing strength of each KL component is adaptive to its corresponding KL eigenvalue, which reflects the SNR of the KL component. The weight in the PWLS objective function is determined by the variance of each measurement, which considers the signal-dependent nature of Poisson noise. To preserve edges in the restored image, an anisotropic quadratic term was used as the penalty in the PWLS objective function. The smoothing strength of the KL domain PWLS filter is controlled by two parameters: the parameter δ in the weight coefficient k'_{jm}, which controls the strength of local smoothing and the smoothing parameter β, which controls the strength of global smoothing.

In the experimental studies, the phantoms were placed on a moving platform that simulates a rigid-body motion. The motion in a real patient is generally nonrigid or deformable. The magnitude of deformable motion varies from voxel to voxel, whereas the motion in a rigid body is uniform across all voxels. Thus, a deformable motion is generally more challenging to handle with regard to registration problems (24). However, the estimation of motion field (or displacement field) between the neighboring images is not required in the presented algorithm. Both the similarity and the difference are modeled through the use of the KL transform. Because of the elimination of voxel-to-voxel registration of the neighboring images, the effectiveness of the method relies largely on the behavior of the principle components of the system. In the deformable case, because the motion occurs only on some parts of the image, the ''average'' motions are actually less compared with the rigid-body motion. When the discrepancy between the two images is small, KLT performance is generally better (25). Therefore, the proposed method should work as well as it does in the case of rigid-body motion investigated in this work. Indeed, KLT has shown excellent performance in noise suppression for four-dimensional (4D) positron emission tomography (16), 4D single photon emission computed tomography (25), and 4D-CT (26) in which deformable motion exists. It is perhaps useful to mention that a potential challenge when dealing with deformable motion is the validation of a fluoroscopic image noise suppression algorithm because of the general lack of the ''ground truth.'' This issue can be partially resolved with the development of a deformable phantom (27, 28) and the use of inherent tissue features (29).

In the presented algorithm, the KLT transform was used to extract correlation information from neighboring images. When neighboring images are not available (*e.g.,* first two image slices) or the correlation between them is weak, the PWLS criterion can be used to suppress noise in the fluoroscopic image through spatial smoothing. The effectiveness of the PWLS criterion in this regard has been proven in noise reduction of cone-beam CT projection data (19, 30) in which the data are equivalent to the X-ray fluoroscopic image. From the results in these studies (19, 30), it is reasonable to conjecture that PWLS criterion without KLT transform can also, to a certain extent, reduce noise in low-dose X-ray fluoroscopy by effectively using the spatial correlation of the voxels within a fluoroscopic image.

In the processed low-dose fluoroscopic image of two phantoms, noise is greatly suppressed, but fine structures are well preserved. Comparison studies with traditional techniques, such as the mean and median filters, show that the proposed algorithm is advantageous in terms of structure preservation. The proposed noise reduction algorithm can significantly improve the quality of low-dose X-ray fluoroscopic imaging and may allow for image acquisition at significantly reduced doses. Given that frequent X-ray imaging is increasingly being used for therapeutic guidance, this work should have an important impact on IGRT clinical practice.

REFERENCES

1. Murphy MJ, Balter J, Balter S, *et al*. The management of imaging dose during image-guided radiotherapy: Report of the AAPM Task Group 75. *Med Phys* 2007;34:4041–4063.

2. Shirato H, Shimizu S, Kunieda T, *et al*. Physical aspects of a real-time tumor-tracking system for gated radiotherapy. *Int J Radiat Oncol Biol Phys* 2000;48:1187–1195.

3. Berbeco RI, Jiang SB, Sharp GC, *et al*. Integrated radiotherapy imaging system (IRIS): design considerations of tumour tracking with Linac gantry-mounted diagnostic x-ray systems with flat-panel detectors. *Phys Med Biol* 2004;49:243–255.
4. Wiersma RD, Weihua M, Xing L. Combined kV and MV imaging for real-time tracking of implanted fiducial markers. *Med Phys* 2008;35:1191–1198.
5. Shirato H, Oita M, Fujita K, *et al*. Feasibility of synchronization of real-time tumor-tracking radiotherapy and intensity-modulated radiotherapy from viewpoint of excessive dose from fluoroscopy. *Int J Radiat Oncol Biol Phys* 2004;60: 335–341.
6. Jabri KN, Wilson DL. Detection improvement in spatially filtered X-ray fluoroscopy image sequences. *J Opt Soc Am A Opt Image Sci Vis* 1999;16:742–749.
7. Aach T, Kunz D. Bayesian motion estimation for temporally recursive noise reduction in X-ray fluoroscopy. *Philips J Res* 1998;51:231–251.
8. Chan CL, Katsaggelos AK, Sahakian AV. Image sequence filtering in quantum-limited noise with applications to low-dose fluoroscopy. *IEEE Trans Med Imaging* 1993;12:610–621.
9. Wilson DL, Jabri KN, Aufrichtig R. Perception of temporally filtered X-ray fluoroscopy images. *IEEE Trans Med Imaging* 1999;18:22–31.
10. Til A, Ulrich S, Gerhard S. Digital image acquisition and processing in medical x-ray imaging. *J Electr Imaging* 1999;8: 7–22.
11. Sanchez-Marin FJ, Srinivas Y, Jabri KN, *et al*. Quantitative image quality analysis of a nonlinear spatio-temporal filter. *IEEE Trans Image Process* 2001;10:288–295.
12. Brailean JC, Kleihorst RP, Efstratiadis S, *et al*. Noise-reduction filters for dynamic image sequences—a review. *Proc IEEE* 1995;83:1272–1292.
13. Xing L, Thorndyke B, Schreibmann E, *et al*. Overview of image-guided radiation therapy. *Med Dosim* 2006;31:91–112.
14. Mao WH, Li TF, Wink N, *et al*. CT image registration in sinogram space. *Med Phys* 2007;34:3596–3602.
15. Hunt BR, Kubler O. Karhunen-Loeve multispectral image-restoration .1. Theory. *IEEE Trans Acoustics Speech Signal Process* 1984;32:592–600.
16. Wernick MN, Infusino EJ, Milosevic M. Fast spatio-temporal image reconstruction for dynamic PET. *IEEE Trans Med Imaging* 1999;18:185–195.
17. Wang J, Li T, Lu HB, *et al*. Penalized weighted least-squares approach to sinogram noise reduction and image reconstruction for low-dose X-ray computed tomography. *IEEE Trans Med Imaging* 2006;25:1272–1283.
18. Wang J, Li T, Lu H, Liang Z. Noise reduction for low-dose single-slice helical CT sinograms. *IEEE Trans Nucl Sci* 2006;53: 1230–1237.
19. Wang J, Li T, Liang Z, *et al*. Dose reduction for kilovoltage cone-beam computed tomography in radiation therapy. *Phys Med Biol* 2008;53:2897–2909.
20. Perona P, Malik J. Scale-space and edge-detection using anisotropic diffusion. *IEEE Trans Pattern Anal Machine Intell* 1990; 12:629–639.
21. Jeffreys H, Jeffreys BS. Methods of mathematical physics, 3rd ed. Cambridge, England: Cambridge University Press; 1988.
22. Maxim PG, Loo BW, Shirazi H, *et al*. Quantification of motion of different thoracic locations using four-dimensional computed tomography: Implications for radiotherapy planning. *Int J Radiat Oncol Biol Phys* 2007;69:1395–1401.
23. Schoonenberg G, Schrijver M, Duan Q, *et al*. Adaptive spatial-temporal filtering applied to X-ray fluoroscopy angiography. *Proc SPIE* 2005;5744:870–878.
24. Schreibmann E, Thorndyke B, Li T, *et al*. Four-dimensional image registration for image-guided radiotherapy. *Int J Radiat Oncol Biol Phys* 2008;71:578–586.
25. Fan Y, Lu H, Liang Z, *et al*. Improved KL domain inversion of the attenuated radon transform for quantitative gated cardiac SPECT. *J Nucl Med* 2007;48:421.
26. Wang J, Li T, Lu H, *et al*. Gain of KL-domain adaptive fbp image reconstruction for 4-D dynamic CT. *2007 IEEE Nuclear Science Symposium Conference Record* 2007;3512–3517.
27. Kashani R, Lam K, Litzenberg D, *et al*. Technical note: A deformable phantom for dynamic modeling in radiation therapy. *Med Phys* 2007;34:199–201.
28. Kashani R, Hub M, Kessler ML, *et al*. Technical note: A physical phantom for assessment of accuracy of deformable alignment algorithms. *Med Phys* 2007;34:2785–2788.
29. Xie Y, Chao M, Xing L. Tissue feature-based and segmented deformable image registration for improved modeling of the shear movement of the lungs. *Int J Radiat Oncol Biol Phys* 2008:conditionally accepted.
30. Zhu L, Wang J, Xing L. Noise suppression in scatter correction for cone-beam CT. *Medical Physics*. Submitted for publication. **Q3**